Received XX Month, XXXX; revised XX Month, XXXX; accepted XX Month, XXXX; Date of publication XX Month, XXXX; date of current version 11 January, 2024.

Digital Object Identifier 10.1109/OJCOMS.2024.011100

Accurate Interference and Coverage Modelling in Finite OWC Networks

Ali Mahbas *(Member, IEEE)*, John Cosmas, Nila Nilavalan, AND Hamed Al-Raweshidy *(Senior Member, IEEE)*

[1]Department of Electronic and Electrical Engineering, College of Engineering, Design and Physical Sciences, Brunel University of London, UB8 3PH Uxbridge, U.K.

CORRESPONDING AUTHOR: Ali Mahbas (e-mail: ali.mahbas@brunel.ac.uk).

This work was supported by the Brunel University of London, U.K.

ABSTRACT Accurate modelling of interference and coverage in optical wireless communication (OWC) systems remains challenging due to the limitations of conventional approaches, which typically rely on infinite-network assumptions or simplified disc-shaped cell models. In practical deployments, OWC networks are finite and regularly structured, resulting in spatially varying interference patterns that are not captured by existing models. This paper proposes a comprehensive analytical framework for evaluating interference and coverage probability in finite OWC networks with regularly deployed grid-based nodes. The framework is developed for a baseline line-of-sight (LOS)-dominant scenario with regularly spaced nodes, ideal transmitter–receiver alignment, and unobstructed propagation conditions (i.e., without blockage or misalignment effects). It explicitly accounts for three-dimensional distances, inter-node spacing, system dimensions, and transmitter–receiver height differences, while incorporating boundary effects. To capture spatial variability, the network is partitioned into core, mid, and boundary zones. Semi-analytical expressions for the interference distribution are derived for each zone, revealing distinct behaviours and pronounced performance degradation in cell-edge regions. Analytical and simulation results demonstrate that commonly adopted disc-assumption models significantly overestimate system performance by neglecting edge effects. For example, at a signal-to-interference-plus-noise ratio (SINR) threshold of -3 dB, disc-based models predict approximately 95% coverage, whereas the proposed framework and simulations show that only about 75% of the core and mid zones satisfy this threshold. The results further show that increasing inter-node distance and adopting higher reuse factors substantially improve coverage, while larger height differences degrade performance by increasing the number of visible interferers. Overall, the proposed framework provides a realistic and generalisable tool for analysing finite OWC networks, enabling more accurate performance evaluation and more reliable network design and deployment.

INDEX TERMS Coverage probability, optical wireless communications (OWC), regular deployment, finite network, interference, signal-to-interference-plus-noise ratio (SINR).

I. INTRODUCTION

OPTICAL wireless communication (OWC) is a high-speed wireless technology that employs optical carriers—infrared, visible light, or ultraviolet—to transmit data. OWC encompasses technologies such as Light Fidelity (Li-Fi) and offers several advantages over conventional radio-frequency (RF) wireless systems, including higher bandwidth and data rates, licence-free spectrum, enhanced security, immunity to RF interference, and the absence of electromagnetic radiation hazards [1]. Accurate modelling of key performance metrics, such as interference and coverage probability, is essential for effective system design and for fully exploiting the potential of OWC systems. Recent studies have highlighted the critical impact of network geometry on system performance, demonstrating that cell-edge regions are particularly susceptible to performance degradation and positioning inaccuracies [2], [3]. Neglecting these regions can prevent OWC networks from meeting future requirements. Motivated by these observations, this work develops an analytical framework that accurately characterises system

This work is licensed under a Creative Commons Attribution 4.0 License. For more information, see https://creativecommons.org/licenses/by/4.0/

performance while explicitly capturing the behaviour of edge regions that are frequently overlooked in existing models.

Both regular and irregular node deployments have been investigated in the literature. Irregular deployments—typically modelled using the Poisson point process (PPP)—have been widely adopted to study various aspects of RF systems [4], [5]. However, such models are often unsuitable for OWC systems due to inherent coverage and performance limitations [6], [7]. A number of studies have nevertheless adopted irregular deployments to analyse interference and coverage probability in OWC systems by modelling node locations as a PPP [10]–[13] or uniform distribution [14]. Node density has also been identified as a key design parameter influencing coverage performance in visible light communication (VLC) systems. For example, [14] investigated the impact of transmitter density on coverage probability in indoor VLC networks, considering factors such as transmitted power and system reliability. The results showed that achieving near-uniform coverage often requires dense transmitter deployments. However, the analysis was based on signal-to-noise ratio (SNR) and assumed the absence of inter-cell interference, which limits its applicability in interference-limited scenarios. [10] analysed outage probability and achievable rate in multi-tier industrial VLC networks using a stochastic-geometry framework in which access points in each tier follow a PPP distribution. Although this study provides useful insights into the effects of field of view (FOV), position, and boundary conditions, its reliance on PPP modelling remains a notable limitation for OWC/VLC networks. Similarly, [12] proposed an analytical model for desired and interference signals in VLC systems and analysed coverage probability under coordinated transmission; however, node deployment was again modelled using a PPP. Likewise, [13] presented a mathematical framework for analysing coverage probability in multi-user VLC systems under a PPP-based spatial distribution, with some nodes assumed to be idle and therefore not contributing interference. Despite their analytical tractability, such irregular deployments are unlikely to meet future system requirements. In practice, OWC systems are typically deployed in structured, deterministic layouts rather than random configurations. Consequently, interference characteristics and performance trends derived from PPP-based models may not accurately reflect realistic deployment scenarios. Moreover, irregular deployments generally provide inferior coverage compared with regular layouts [6], [15].

Regular deployments are therefore considered more promising for realising the full capabilities of OWC systems; however, their analytical complexity remains a major challenge [2]. To manage this complexity, many studies introduce simplifying assumptions or reduced-order models when analysing regular deployments. While these approaches improve tractability, they often compromise accuracy and limit applicability to practical systems. Common examples include fixed-distance assumptions, single-cell models, and disc-shaped cell approximations in multi-node deployments. Several studies assume that user equipment (UE) is located at a fixed distance from the serving node [16]–[19]. For instance, [16] proposed an energy-efficient client-side access-point selection strategy for hybrid wireless fidelity (WiFi)–LiFi networks, demonstrating improvements in quality-of-service (QoS) provisioning and energy consumption compared with conventional approaches. The study also examined uplink power adaptation to further enhance internet-of-things (IoT) device efficiency. However, a key limitation of this work is the assumption that UE is located at a fixed distance from the access point, which restricts the applicability of the results by neglecting spatial variability in UEs' locations. In [17], interference in regular deployments was analysed by considering inter-cell distance and FOV, under the assumption that UE of interest is positioned at a fixed distance from all nodes. In [18], a method was proposed to simultaneously reduce interference from multiple sources and improve coverage in indoor VLC systems. This approach assumed that the receiver can estimate its location and orient itself toward the closest node to maximise the desired signal while minimising interference. Similarly, [19] examined the nonlinear effects of light-emitting diodes (LEDs) on the trade-off between energy efficiency and spectral efficiency when using direct-current-biased optical orthogonal frequency-division multiplexing (OFDM), again assuming that UE is located at a fixed distance from the serving node. Although fixed-distance assumptions are useful for highlighting the influence of specific system parameters, they provide only limited insight into UE spatial distributions and overall network geometry. In particular, they fail to capture the spatially varying interference conditions that arise across different locations within a practical system.

Furthermore, some studies adopt a single-cell model in which UEs are located within a single cell, with no interference from neighbouring nodes and no constraints imposed by adjacent cells. In such models, the cell footprint is typically assumed to be circular, resulting in a three-dimensional (3D) conical coverage region [8], [9], [26]–[28]. For example, [8] investigated the probability distribution of the VLC channel-gain difference (CGD) under a Lambertian radiation model. Due to analytical complexity, approximate expressions were derived, and UE locations were assumed to be uniformly distributed within the cell. In [26], secrecy performance was analysed for a VLC system with one legitimate receiver and multiple eavesdroppers. By modelling the randomness of receiver and eavesdropper locations, the statistical properties of the downlink SNR were characterised, and closed-form expressions for secrecy outage probability were derived. However, the analysis relied on a circular single-cell model and considered SNR-based outage only, neglecting interference. Similarly, [27] studied secure transmission in indoor VLC systems with simultaneous lightwave information and power transfer, assuming a single-cell circular model with two randomly located UEs. Although a protected-zone

scheme was proposed to enhance physical-layer security, the single-cell assumption prevented the model from capturing distance variability and interference effects inherent to multicell deployments. In addition, [28] analysed outage probability and energy harvesting in VLC downlink systems employing non-orthogonal multiple access (NOMA) with an RF uplink, assuming terminals were randomly distributed within a single hemispherical cell. Likewise, [9] examined NOMA in VLC downlink systems under guaranteed QoS and best-effort service scenarios, analytically characterising coverage probability and ergodic sum rate. Although the influence of LED semi-angles was highlighted, the analysis again relied on a circular single-cell model and ignored inter-cell interference. As in many of the aforementioned studies, the absence of neighbouring cells limits the applicability of the results, since practical OWC deployments inherently involve overlapping illumination regions and significant inter-cell interference. While the circular-cell assumption is reasonable within isolated single-cell models, it does not hold in realistic regular deployments. Practical OWC systems consist of multiple cells arranged in grid-based layouts, where each cell's footprint is constrained to a square or another tiling geometry rather than a circle. Consequently, single-cell models provide only limited insight into the overall network geometry and its impact on system performance.

It is widely recognised that multicell models provide a more realistic framework for analysing system performance—such as interference characteristics and coverage probability—because they account for inter-cell constraints and the relative positions of system nodes. Several studies have examined system performance while explicitly considering distances between UEs and system nodes [6], [9], [20]–[25]. For example, [6] proposed a mathematical model to evaluate downlink performance in VLC systems, analysing outage probability and signal-to-interference-plus-noise ratio (SINR) under both regular and irregular deployments. The results showed that regular deployments outperform PPP-based configurations and that well-designed OWC systems can exceed RF networks in indoor data rates. However, several simplifying assumptions limit accuracy. In particular, interference in an infinite network was approximated using only the first tier of hexagonal interferers, following the flower-model approximation in [20]. Moreover, although the deployment was hexagonal, each cell was further simplified to a circular shape, neglecting edge effects where geometry strongly influences performance [2]. In [21], interference mitigation using angle-diversity receivers (ADRs) was investigated. Each photodiode was assumed to capture one line-of-sight (LOS) signal, while interference collected by other photodiodes was treated as non-line-of-sight (NLOS). While valid for narrow FOVs or low node densities, this assumption becomes less accurate in dense deployments. As in [6], the hexagonal deployment was again approximated using circular cells. Similarly, [22] analysed SINR distributions in multicell VLC networks employing ADRs and various signal-combining schemes, again relying on a circular-cell approximation. The cell of interest was partitioned into a central disc and an outer ring, which introduces geometric inaccuracies. When the ring radius is set to $d/2$, where d is the inter-node distance, portions of the true cell-edge region are omitted. Conversely, larger disc radii incorrectly include areas from neighbouring cells. As a result, the derived SINR behaviour may not accurately reflect true interference patterns, particularly at cell edges. Furthermore, SINR was characterised only at the cell centre and edge, even though it also depends on the UE's angular position relative to the serving node—a dependence demonstrated later in this paper. A similar simplification was adopted in [23]. In [24], quality-of-experience (QoE) coverage probability was analysed for VLC systems under different multiple-access schemes and terminal densities. However, to maintain analytical tractability, all cells were modelled as circular, again ignoring realistic geometric constraints. The study in [25] incorporated 3D UE positioning by modelling truncated conic coverage volumes, but the regular deployment was still simplified to circular cell footprints. Moreover, outage probability was defined in terms of SNR only, neglecting inter-cell interference.

Despite the extensive body of work on OWC system modelling, important limitations remain in existing approaches. PPP-based models, while analytically tractable, fail to capture the structured and deterministic nature of practical OWC deployments. Similarly, studies based on regular layouts often rely on simplifying assumptions such as infinite network size, regular grids with circular-cell approximations, or reduced-order interference models, which can lead to inaccuracies in representing realistic system behaviour. In particular, these approaches typically overlook the impact of finite network dimensions, exact cell geometry, and boundary effects, all of which play a critical role in shaping interference and coverage performance. In contrast, this work develops a comprehensive analytical framework for finite, regularly deployed OWC networks that explicitly accounts for these factors. By accurately modelling system geometry, inter-node distances, and spatial variations across different regions—including cell-edge areas—the proposed framework provides a more realistic and generalisable characterisation of interference and coverage probability than existing methods.

Motivated by these limitations, this paper derives key performance metrics—such as interference and coverage probability—for a finite OWC network in which both the distribution and strength of desired and interfering signals vary due to system boundaries. We provide a detailed analysis of cell regions while explicitly accounting for 3D distance variations and edge effects. To the best of our knowledge, the proposed framework is the first to model system performance in a finite, regular OWC deployment while accurately capturing the combined impact of inter-node distance, system dimensions, and height differences.

The main contributions of this paper are summarised as follows:

- We propose a general analytical framework for evaluating system performance in finite OWC networks with regularly deployed nodes. The expected interference at a randomly located UE is derived by explicitly accounting for 3D distances to serving and interfering nodes, node density (inter-node distance), and system dimensions.
- We demonstrate that interference exhibits strong spatial variability due to boundary effects. To capture this behaviour, the network is partitioned into three zones—core, mid, and boundary—each characterised by distinct interference conditions.
- We derive the interference distribution in the core zone by incorporating key parameters such as distances to interfering nodes, height differences, number of interferers, and angular separation. We show that distance and angular parameters (e.g., r_0 and α) become correlated in the cell-edge region, leading to distinct interference characteristics compared with the cell centre.
- We extend the analysis to the mid zone, where the interference distribution retains a similar analytical structure but with reduced magnitude due to a smaller number of effective interferers.
- We characterise the boundary zone, where both the number of interferers and their geometric configuration differ significantly from the core and mid zones. Boundary cells are shown to consist of multiple regions with distinct interference distributions, depending on the relative distance between the last node and the system boundary.
- We extend the framework to incorporate interference mitigation through frequency reuse, demonstrating how higher reuse factors alter the interference structure and improve system performance.
- We derive the coverage probability, defined as the probability that the received SINR exceeds a given threshold. The analysis is performed at multiple spatial levels (system-wide, zone-wise, and subregion-wise), revealing detailed spatial performance variations and identifying regions most susceptible to degradation.

For ease of reference, the main symbols used throughout the paper are summarised in Table 1.

The remainder of this paper is organized as follows. Section II describes the system model and presents the different zones in a finite regular deployment. Section III derives the interference for different cell areas and system zones. In Section IV, the coverage probability is investigated. Section V validates the accuracy of the analysis through simulations. Finally, conclusions are drawn in Section VI.

TABLE 1. Main symbols used in the paper.

Symbol	Description
h_n	Node height
h_c	Coverage height / maximum UE height
h	Vertical distance between node plane and UE
d	Inter-node spacing
$\acute{d}$	Width of the boundary zone
w_s, l_s	Network width and length
$N_0, N_{t,\Psi_\star}$	Serving node and interfering node in tier t at angle $\Psi_\star$
L_0	Baseline connecting N_0 to $N_{1,0}$
$\Psi_\star$	Angular location of an interferer
$D_{t,\Psi_\star}$	Distance between N_0 and $N_{t,\Psi_\star}$
$T, \acute{T}$	Number of tiers for reuse factors 1 and 3
$r_0, r_{t,\Psi_\star}$	Horizontal distances between UE and N_0, and between UE and $N_{t,\Psi_\star}$
α	Angle between r_0 and the baseline L_0
R_0	3D distance between UE and the serving node
θ_t, θ_r	Semi-angle at half-power and receiver FOV
ϕ_t, ϕ_r	Irradiance angle at the transmitter and incidence angle at the receiver
A_{det}	Detector area
G_{con}, T_s	Optical concentrator gain and optical filter gain
$\Gamma(r)$	FOV constraint function
μ	Lambertian order
$G_0, G_{t,\Psi_\star}$	Serving and interfering channel gains
P_t	Transmit optical power
K	Constant defined as $K = \frac{P_t(\mu+1)A_{det}G_{con}T_s}{2\pi}$
w_m	Width of the mid zone
$\mathcal{P}^z$	Probability of zone z
I	Overall interference
I^z	Interference in zone z
I^z, I^{z3}	Interference in zone z reuse factors 1 and 3
I_a^z	Interference in region a of zone z
$C^z_{t,\Psi_\star}, E^z_{t,\Psi_\star}$	Interference contribution from $N_{t,\Psi_\star}$ in the centre and edge regions of the cell
S	Desired signal
$\mathcal{CP}$	Overall coverage probability
$\mathcal{CP}^z$	Coverage probability in zone z
SINR^z	Signal-to-interference-plus-noise ratio in zone z
γ	SINR threshold
σ^2	Noise variance
η	Noise power spectral density
BW	Bandwidth
$\mathbb{D}_a^z$	Spatial domain of region a in zone z
$f_a^z(x)$	PDF of variable x in region a of zone z

II. System Model

We consider a regular OWC system with a square layout, where nodes are mounted on the ceiling at a fixed height h_n and separated by an inter-node spacing d, as illustrated in Fig. 1. The network covers a finite area of size $w_s \times l_s$, where w_s and l_s denote the system width and length, respectively.

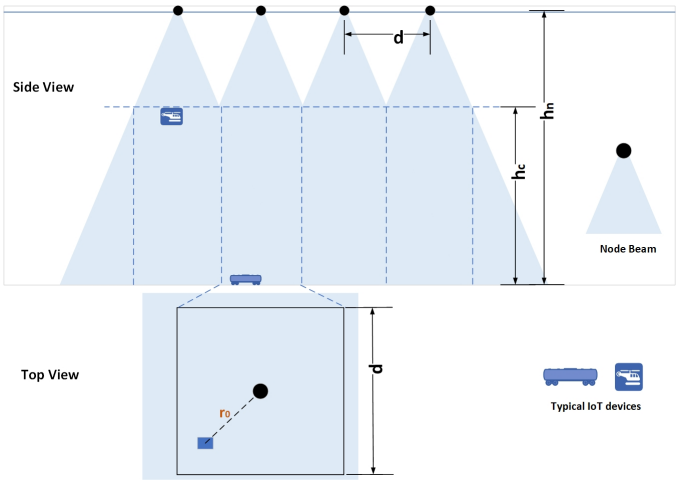

FIGURE 1. OWC System.

UEs are randomly distributed within this area, including near the edges. To ensure full coverage up to a maximum height h_c, beams from adjacent nodes overlap. Although each node generates a conical optical beam, the effective coverage region of a cell forms a square prism of dimensions $d \times d \times h_c$, dictated by connection requirements and the presence of neighbouring nodes at distance d. In OWC systems, the communication channel between a node and UE consists of LOS and NLOS components produced by reflections from interior surfaces. However, in typical environments, the NLOS component is significantly weaker than the LOS component [12], [29]–[31], and is therefore neglected in this analysis. Furthermore, the analysis assumes ideal transmitter–receiver alignment and an unobstructed LOS path between the node and UE. Under these assumptions, blockage effects (e.g., due to obstacles or human movement) and misalignment effects (e.g., due to device orientation) are not explicitly modelled. This baseline scenario enables tractable analysis and isolates the impact of network geometry, inter-node spacing, and interference in finite regular deployments.

The height difference between UE and the node plane is assumed to vary within the range $[0, h_c]$, reflecting practical usage scenarios such as handheld devices, devices placed on furniture, or aerial platforms. Accordingly, the vertical distance between the transmitter plane and UE is defined as $h \in [h_n - h_c, , h_n]$ and is modelled as a random variable to capture the 3D spatial distribution of UEs. The channel gain between UE and the closest (serving) node N_0 is expressed as:

$$G_0 = \frac{(\mu+1)A_{det}\cos^{\mu}(\phi_t)\cos(\phi_r)G_{con}T_s}{2\pi R_0^2}\Gamma(r_0) \quad (1)$$

where $\mu = -\log_{10}(2)/\log_{10}(\cos(\theta_t))$ is the Lambertian order of emission, θ_t is the transmitter semi-angle at half-power, A_{det} is the physical area of the detector, ϕ_t and ϕ_r denote the transmitter and receiver alignment angles, G_{con} is the optical concentrator gain, T_s is the optical filter gain, R_0 is the 3D distance between UE and N_0, r_0 is the horizontal distance between the centre of the serving cell and UE, h is the vertical separation, and $\Gamma(r_0)$ is the FOV constraint function:

$$\Gamma(r_0) = \begin{cases} 1 & r_0 \le h\tan(\theta_r) \\ 0 & \text{otherwise} \end{cases} \quad (2)$$

where θ_r denotes the photodetector (PD) FOV, i.e., the maximum incidence angle at which the signal can be detected. It is assumed that UE is always covered by the closest node N_0. This is to ensure full coverage within the system, hence $\Gamma(r_0) = 1$. It is also assumed perfect alignment between transmitters and receivers: nodes point downward at 90° to the ceiling, and UEs point upward at 90° to the floor. Under this assumption, $\cos(\phi_t) = \cos(\phi_r) = h/R_0$, and the channel gain becomes:

$$G_0 = \frac{(\mu+1)A_{det}G_{con}T_s h^{\mu+1}}{2\pi R_0^{\mu+3}} \quad (3)$$

Since a finite network is considered, several additional aspects arise. When UE is located near the system centre (core zone), interference is received from all directions due to symmetry. As UE moves toward the boundary—within the mid and boundary zones—the number of interfering nodes decreases. Furthermore, in the boundary zone, both the number of interferers and the distance distributions of serving and interfering nodes change due to the finite geometry. In order to characterise the interference accurately, the network is divided into the three zones shown in Fig. 2:

- **Boundary zone**: The region adjacent to the outer edges of the network, extending from the last row of nodes to the system boundary. In this zone, UE experiences fewer interfering nodes due to the finite network extent.
- **Mid zone**: The intermediate region between the boundary and core zones. It contains cells within a horizontal distance of $h\tan(\theta_r)$ from the last row of nodes. UEs in this zone receive interference from a subset of surrounding nodes, with interference gradually increasing toward the core.
- **Core zone**: The central region of the network, consisting of cells whose horizontal distance from all boundaries exceeds $h\tan(\theta_r)$. In this zone, UE experiences full interference from all directions due to the network's effective symmetry.

The probability that UE lies in the boundary zone is:

$$\mathcal{P}^b = \frac{2\acute{d}(w_s + l_s - \acute{d})}{w_s l_s} \quad (4)$$

where $\acute{d}$ is the width of the boundary zone (distance between the last row and the system boundary) $2\acute{d}(w_s + l_s - \acute{d})$ is the boundary area, and $w_s l_s$ is the total network area. Since the core and mid zone widths depend on the UE height, the corresponding probabilities also depend on h.

The probability that UE lies in the mid zone is:

$$\mathcal{P}^m = \frac{2(w_m + \acute{d})(w_s + l_s - w_m - \acute{d}) - 2\acute{d}(w_s + l_s - \acute{d})}{w_s l_s} \tag{5}$$

where $2(w_m + \acute{d})(w_s + l_s - w_m - \acute{d})$ represents the area of both mid and boundary zones and, w_m is the mid-zone width and obtained by:

$$w_m = (T-1)d + \frac{d}{2}. \tag{6}$$

where T denotes the total number of interference tiers, as derived in Theorem 1:

$$T = 2\left\lfloor \frac{\frac{2h_n \tan(\theta_r)}{d} - 1}{2} \right\rfloor + 1 \tag{7}$$

where $\lfloor \cdot \rfloor$ represents the floor function, h_n is the height of the nodes (see Fig. 2). The maximum value of $\mathcal{P}^m$ occurs when $h = h_n$, and the minimum occurs when $h = h_n - h_c$. The probability that UE lies in the core zone follows as:

$$\mathcal{P}^c = 1 - \mathcal{P}^b - \mathcal{P}^m. \tag{8}$$

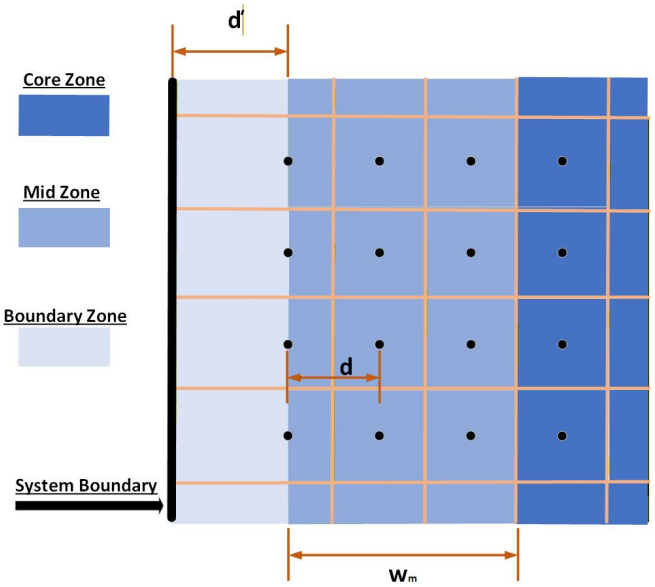

FIGURE 2. Finite system: core zone, mid zone and boundary zone.

III. Interference

Before presenting the mathematical derivations, it is useful to summarise the key ideas underlying this section. The interference experienced by a randomly located UE in a finite OWC network is governed by three main factors: the UE's location within the overall network, its position within the serving cell, and the adopted reuse factor. First, due to the finite system geometry, UEs in the core, mid, and boundary zones experience different sets of interfering nodes. In particular, UEs in the core zone are surrounded by interferers in all directions, whereas UEs in the mid and boundary zones experience reduced interference due to the absence of nodes beyond the system boundaries. Second, even within the same zone, interference varies between the cell-centre and cell-edge regions because the distances to the serving and interfering nodes depend on the UE location. Third, the reuse factor determines the set of active interferers by increasing the separation between nodes using the same resources, thereby reducing interference. Based on these observations, the analysis in this section derives the interference for each zone and subregion, and subsequently extends the framework to account for higher reuse factors. The expected interference experienced by UE randomly located in a finite network can be expressed by:

$$I = \mathcal{P}^c I^c + \mathcal{P}^m I^m + \mathcal{P}^b I^b. \tag{9}$$

where I^c, I^m and I^b are the interference experienced by UE given it is located in the core, mid and boundary zone respectively. $\mathcal{P}^c$, $\mathcal{P}^m$ and $\mathcal{P}^b$ are obtained in Eq. (8), Eq. (5) and Eq. (4) respectively. Note that I^c, I^m and I^b are addressed in the next subsections.

For completeness, we briefly summarise several standard probability concepts and notation used throughout the derivations. These are included for clarity and consistency, and are not part of the novel contributions of this work.

Definition 1 (CDF and PDF): Let $\mathcal{A}$ denote the total area of interest, centred at $\mathcal{Y}$. The cumulative distribution function (CDF) $F(x)$ is defined as the probability that a randomly chosen point lies within a radius x of $\mathcal{Y}$:

$$\begin{aligned} F(x) &= \mathbb{P}(\mathcal{X} \leq x) \\ &= \frac{\mathbb{D}(\mathcal{Y}, x) \cap \mathcal{A}}{\mathcal{A}} \end{aligned}$$

where $\mathbb{D}(\mathcal{Y}, x)$ is a disc of radius x centred at $\mathcal{Y}$. The corresponding probability density function (PDF) is:

$$f(x) = \frac{d}{dx} F(x).$$

Remark: $F(x)$ represents the fraction of the total area within distance x from $\mathcal{Y}$, while $f(x)$ represents the likelihood of a randomly chosen point being located at distance x.

Definition 2 (Independence): If $\mathcal{X}$, $\mathcal{Y}$, and $\mathcal{Z}$ are independent random variables, their joint PDF is:

$$f_{\mathcal{X},\mathcal{Y},\mathcal{Z}}(x, y, z) = f_{\mathcal{X}}(x)\, f_{\mathcal{Y}}(y)\, f_{\mathcal{Z}}(z).$$

Remark: Independence allows the joint distribution to be expressed as the product of marginal distributions, which simplifies the analysis.

Definition 3 (Linearity of Expectation): For any random variables $\mathcal{X}_1, \mathcal{X}_2, \ldots, \mathcal{X}_y$, the expected value of their sum equals the sum of their expectations:

$$\mathbb{E}\left[\sum_{i=1}^{y} \mathcal{X}_i\right] = \sum_{i=1}^{y} \mathbb{E}[\mathcal{X}_i].$$

Remark: This property holds regardless of independence and is fundamental for computing expected interference as a sum of contributions from multiple nodes.

Definition 4 (Joint PDF): Let $\mathcal{X}$ and $\mathcal{Y}$ be random variables

with conditional PDF $f_{\mathcal{X}|\mathcal{Y}}(x|y)$ and marginal PDF $f_{\mathcal{Y}}(y)$. Then their joint PDF is:

$$f_{\mathcal{X},\mathcal{Y}}(x,y) = f_{\mathcal{X}|\mathcal{Y}}(x|y) f_{\mathcal{Y}}(y),$$

and equivalently:

$$f_{\mathcal{X},\mathcal{Y}}(x,y) = f_{\mathcal{Y}|\mathcal{X}}(y|x) f_{\mathcal{X}}(x).$$

Remark: This relationship allows joint distributions to be expressed in terms of conditional and marginal PDFs, which is useful for analysing interference with location-dependent effects.

A. Network Core Zone

This area comprises the cells located at the centre of the network, where interference is generated by nodes symmetrically distributed around the serving cell. Interfering nodes may belong to different tiers, defined as concentric rings of cells surrounding the serving node. For example, the first tier consists of eight nodes immediately adjacent to the serving node, the second tier includes the next ring of nodes, and so on. The number of interfering tiers depends on the UE's location, height, and FOV. In this paper, the straight line connecting the serving node N_0 to the closest interferer $N_{1,0}$ on the UE's plane is denoted as the baseline (L_0). The angle α is defined as the angle between r_0 and the baseline L_0, and it can take values in the range $[0, \frac{\pi}{4}]$. Each node in the interfering tiers is denoted by $N_{t,\Psi_\star}$, where t represents the tier index and $0 \leq \Psi_\star \leq 2\pi$ denotes the anti-clockwise angle between L_0 and the straight line connecting N_0 to $N_{t,\star}$ ($D_{t,\Psi_\star}$). For instance, the closest interfering node is denoted by $N_{1,0}$, as it belongs to the first tier and lies on L_0, while the closest node from the second tier is denoted by $N_{2,0}$ as shown in Fig. 3. Note that both $\Psi_\star$ and $D_{T,\Psi_\star}$ are deterministic and depend solely on the network geometry. For example, in the first tier ($t = 1$), the interfering nodes include $N_{1,0}$, $N_{1,\frac{\pi}{4}}$, $N_{1,\frac{\pi}{2}}$, $N_{1,\frac{3\pi}{4}}$, $N_{1,\pi}$, $N_{1,\frac{5\pi}{4}}$, $N_{1,\frac{3\pi}{2}}$, and $N_{1,\frac{7\pi}{4}}$. These nodes are located at distances $D_{1,0} = d$, $D_{1,\frac{\pi}{4}} = d\sqrt{2}$, $D_{1,\frac{\pi}{2}} = d$, $D_{1,\frac{3\pi}{4}} = d\sqrt{2}$, $D_{1,\pi} = d$, $D_{1,\frac{5\pi}{4}} = d\sqrt{2}$, $D_{1,\frac{3\pi}{2}} = d$, and $D_{1,\frac{7\pi}{4}} = d\sqrt{2}$ from N_0, respectively. Furthermore, the distances between UE and nodes in the first tier are random variables given by $r_{1,0} = \sqrt{r_0^2 + d^2 - 2r_0 d\cos(0-\alpha)}$, $r_{1,\frac{\pi}{4}} = \sqrt{r_0^2 + 2d^2 - 2\sqrt{2}r_0 d\cos(\frac{\pi}{4}-\alpha)}$ $\cdots$ $r_{1,\frac{7\pi}{4}} = \sqrt{r_0^2 + 2d^2 - 2\sqrt{2}r_0 d\cos(\frac{7\pi}{4}-\alpha)}$.

The channel gain between node $N_{t,\Psi_\star}$ and UE is obtained similar to Eq. (1):

$$G_{t,\Psi_\star} = \frac{(\mu+1)A_{det}G_{con}T_s h^{\mu+1}\Gamma(r_{t,\Psi_\star})}{2\pi R_{t,\Psi_\star}^{\mu+3}} \tag{10}$$

where $\Gamma(r_{t,\Psi_\star})$ is obtained by

$$\Gamma(r_{t,\Psi_\star}) = \begin{cases} 1 & r_{t,\Psi_\star} \leq h\tan(\theta_r) \\ 0 & \text{otherwise} \end{cases} \tag{11}$$

Moreover, the interference experienced by UE depends on its location within the serving cell. UEs are therefore expected to experience different interference levels based on their intra-cell position. For example, UE located at the centre of the cell may be at different distances from the serving and interfering nodes compared to UE at the cell edge, resulting in distinct interference levels. These differences arise from the varying distributions of geometric parameters across different regions of the cell. In this work, the spatial distribution of UE within the cell is captured through area-weighted joint densities, whose supports correspond to specific subregions (e.g., centre and edge). As a result, the expected interference in the core zone is obtained as the sum of the contributions from these subregions:

$$\mathbb{E}[I^c] = \mathbb{E}[I_c^c] + \mathbb{E}[I_e^c] \tag{12}$$

where $\mathbb{E}[I_c^c]$ and $\mathbb{E}[I_e^c]$ represent the spatially weighted contributions to the expected interference from the cell-centre and cell-edge regions, respectively, within the core zone. These terms inherently account for the relative likelihood of UE being located in each subregion through the integration of the corresponding joint densities over their respective domains. The expressions for $\mathbb{E}[I_c^c]$ and $\mathbb{E}[I_e^c]$ are derived in Theorems 1 and 2, respectively.

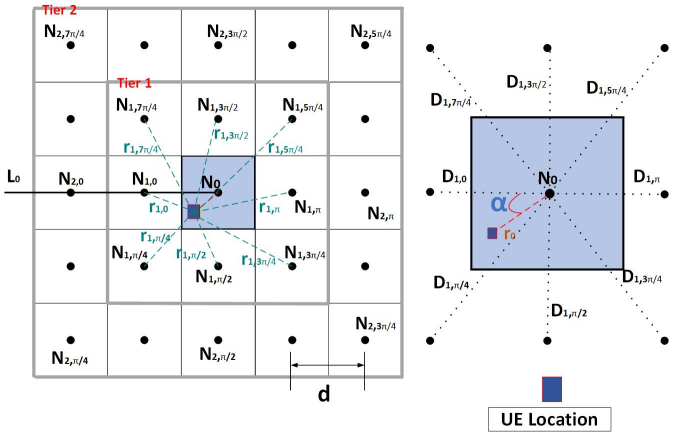

FIGURE 3. Cell of interest.

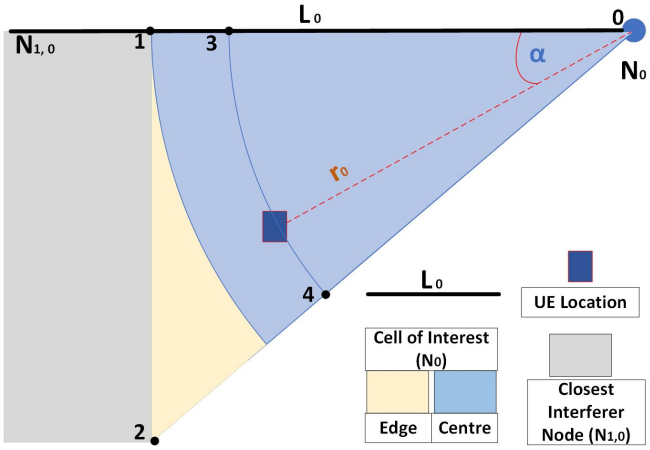

FIGURE 4. Core zone - Cell centre.

Theorem 1: The contribution to the expected interference in the core zone from the cell-centre region, corresponding to UE locations with $0 \leq r_0 \leq \frac{d}{2}$, is given by:

$$\mathbb{E}[I_c^c] = \int_{\mathbb{D}_c^c} I_c^c(r,h,\alpha)\ f_c^c(r,h,\alpha)\, d\mathbb{D}_c^c \tag{13}$$

where $\mathbb{D}_c^c$ denotes the bounded spatial domain of the cell-centre region in the core zone (r_0, α and h). Specifically, $0 \leq r_0 \leq \frac{d}{2}$ is the horizontal distance between UE and the centre of serving cell, $h_n - h_c \leq h \leq h_n$ is the height difference between UE and the serving node, and $0 \leq \alpha \leq \frac{\pi}{4}$ is the angle between r_0 and the baseline L_0. The term $I_c^c(r,h,\alpha)$ denotes the analytical expression of the interference in the cell-centre region as a function of the distance-dependent parameters r, h, and α, arising from the set of potential interfering nodes, and is given by:

$$\begin{aligned} I_c^c(r,h,\alpha) &= I_{c(T-1)}^c + I_{c(T)}^c \\ &= I_{c(T-1)}^c + \sum_{i=1}^{4} \left(C_{T,\Psi_{i1}}^c + C_{T,\Psi_{i2}}^c\right) \\ &\quad + \sum_{t=1}^{T-1}\sum_{m=1}^{4} \left(C_{T,\Psi_{tm1}}^c + C_{T,\Psi_{tm2}}^c\right) \end{aligned} \tag{14}$$

where $I_{c(T-1)}^c$ and $I_{c(T)}^c$ denote the interference contributions from the first $T-1$ tiers and the T-th tier, respectively, $C_{T,\Psi_\star}^c = Kh^{\mu+1}(r_{T,\Psi_{i1}}^2 + h^2)^{-\frac{\mu+3}{2}}\Gamma(r_{T,\Psi_{i1}})$ represents the interference at the cell centre of interest from a node $N_{T,\Psi_\star}$ located at a distance $r_{T,\Psi_\star}$. $C_{T,\Psi_{i1}}^c = Kh^{\mu+1}(r_{T,\Psi_{i1}}^2 + h^2)^{-\frac{\mu+3}{2}}\Gamma(r_{T,\Psi_{i1}})$, $C_{T,\Psi_{i2}}^c = Kh^{\mu+1}(r_{T,\Psi_{i2}}^2 + h^2)^{-\frac{\mu+3}{2}}\Gamma(r_{T,\Psi_{i2}})$, $C_{T,\Psi_{tm1}}^c = Kh^{\mu+1}(r_{T,\Psi_{tm1}}^2 + h^2)^{-\frac{\mu+3}{2}}\Gamma(r_{T,\Psi_{tm1}})$, and $C_{T,\Psi_{tm2}}^c = Kh^{\mu+1}(r_{T,\Psi_{tm2}}^2 + h^2)^{-\frac{\mu+3}{2}}\Gamma(r_{T,\Psi_{tm2}})$. Note that $r_{T,\Psi_{i1}} = \sqrt{r_0^2 + (Td)^2 - 2r_0Td\cos(\Psi_{i1}-\alpha)}$ and $r_{T,\Psi_{i2}} = \sqrt{r_0^2 + 2(Td)^2 - 2\sqrt{2}r_0Td\cos(\Psi_{i2}-\alpha)}$, $r_{T,\Psi_{tm1}} = \sqrt{r_0^2 + D_{T,\Psi_{tm}}^2 - 2r_0D_{T,\Psi_{tm}}\cos(\Psi_{tm1}-\alpha)}$, $r_{T,\Psi_{tm2}} = \sqrt{r_0^2 + D_{T,\Psi_{tm}}^2 - 2r_0D_{T,\Psi_{tm}}\cos(\Psi_{tm2}-\alpha)}$ are the distances between UE and the nodes $N_{1,\Psi_{i1}}$, $N_{1,\Psi_{i2}}$, $N_{1,\Psi_{tm1}}$ and $N_{1,\Psi_{tm2}}$ located at angles of $\Psi_{i1} = \frac{(i-1)\pi}{2}$ and $\Psi_{i2} = \frac{\pi}{4} + \frac{(i-1)\pi}{2}$, $\Psi_{tm1} = \frac{(m-1)\pi}{2} + \tan^{-1}(\frac{t}{T})$, and $\Psi_{tm2} = \frac{m\pi}{2} - \tan^{-1}(\frac{t}{T})$ in respect to L_0, $D_{T,\Psi_{tm}} = \sqrt{(T^2+t^2)}d$ and T being the total number of tiers contributing interference:

$$T = 2\left\lfloor \frac{\frac{2h_n\tan(\theta_r)}{d} - 1}{2} \right\rfloor + 1 \tag{15}$$

$\lfloor \dots \rfloor$ is the floor function. Given that UE is located in the core zone, the joint density of the random variables r_0, h, and α, whose support corresponds to the cell-centre region, is given by:

$$f_c^c(r,h,\alpha) = \frac{8r}{d^2h_c} \tag{16}$$

Note that this density is defined over the entire core zone with support restricted to the cell-centre region. Therefore, its integral over the corresponding domain yields the spatial probability of UE being located in the cell-centre region, rather than unity.

Proof: See Appendix A ■

It is believed that the distributions of the main parameters at the cell edge differ from those at the centre. Therefore, a careful investigation is necessary to accurately model the interference at the cell edge. The interference caused by the interferer nodes at the edge of the cell of interest is presented in the following theorem.

Theorem 2: The contribution to the expected interference in the core zone from the cell-edge region, corresponding to UE locations with $\frac{d}{2} < r_0 \leq \frac{d}{\sqrt{2}}$, can be expressed as:

$$\mathbb{E}[I_e^c] = \int_{\mathbb{D}_e^c} I_e^c(r,h,\alpha)\ f_e^c(r,h,\alpha)\, d\mathbb{D}_e^c \tag{17}$$

where $\mathbb{D}_e^c$ is the bounded spatial domain of the cell-edge region in the core zone (r_0, α and h). Specifically, $\frac{d}{2} < r_0 \leq \frac{d}{\sqrt{2}}$ is the horizontal distance between UE and the centre of serving cell, $h_n - h_c \leq h \leq h_n$ is the height difference between UE and the serving node, and $\alpha_{min} \leq \alpha \leq \alpha_{max}$ is the angle between r_0 and the baseline L_0, $\alpha_{min} = \cos^{-1}\left(\frac{d}{2r}\right)$ is the minimum value that α can take when UE is at r_0 from the centre of cell of interest and $\alpha_{max} = \frac{\pi}{4}$. The term $I_e^c(r,h,\alpha)$ denotes the analytical expression of the interference in the cell-edge region as a function of the distance-dependent parameters r, h, and α, arising from the set of potential interfering nodes. It has the same analytical structure as that in the cell-centre region, i.e., $I_c^c(r,h,\alpha) = I_e^c(r,h,\alpha)$, where $I_c^c(r,h,\alpha)$ is derived in Theorem 1. However, this equality refers to the analytical form of the interference expression and does not imply identical interference values. The actual interference experienced by UE in the cell-edge region differs due to variations in the distance-dependent parameters r_0, h, and α, as well as the spatial weighting introduced by the corresponding densities. Given that UE is located in the core zone, the joint density of the random variables r_0, h, and α, whose support corresponds to the cell-edge region, is given by:

$$f_e^c(r,h,\alpha) = \frac{\left(2r\pi - 8r\cos^{-1}\left(\frac{d}{2r}\right)\right)}{h_c\left(\alpha_{max} - \alpha_{min}\right)d^2} \tag{18}$$

Note that this density is defined over the entire core zone with support restricted to the cell-edge region. Therefore, its integral over the corresponding domain yields the spatial probability of UE being located in the cell-edge region, rather than unity.

Proof: See Appendix B ■

Note that the result in Eq. (12) can also interpreted as the expected interference under the assumption of an infinite system. However, in practice, the system is finite, and UEs may also be located in different regions, such as the mid and boundary zones. In the next two subsections, the interference in these zones is analysed.

The results in Theorems 1 and 2 provide insight into the interference behaviour in the core zone, where the network

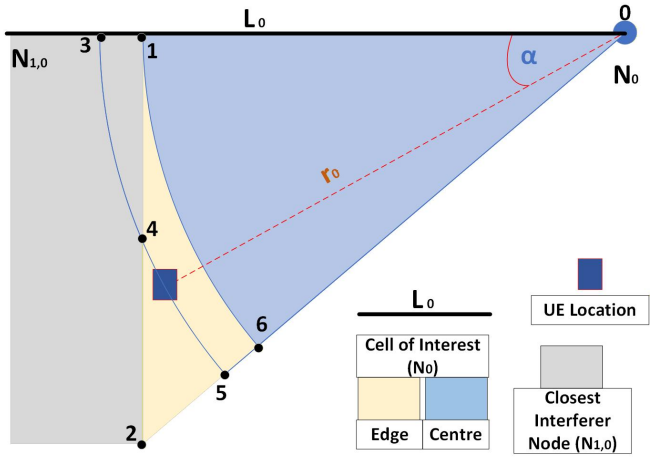

FIGURE 5. Core zone - Cell edge.

exhibits full geometric symmetry and is unaffected by system boundaries. In this zone, the interference experienced by the UE depends strongly on the distance-dependent parameters r_0, α, and h, which jointly determine the relative position of the UE with respect to the serving and interfering nodes. In the cell-centre region ($0 \leq r_0 \leq \frac{d}{2}$), the parameters r_0 and α are weakly coupled and follow simple geometric distributions, with $\alpha \in [0, \frac{\pi}{4}]$. This results in more uniform interference characteristics, as captured in Theorem 1. In contrast, in the cell-edge region ($\frac{d}{2} < r_0 \leq \frac{d}{\sqrt{2}}$), these parameters become coupled due to geometric constraints, leading to a dependence of the angular range on r_0, as reflected in Theorem 2. Consequently, UEs in the edge region are not only located farther from their serving node but are also closer to multiple interferers, resulting in higher interference levels. The system parameters further influence these behaviours. Increasing the transmitter–receiver height difference expands the footprint of each cell and increases the number of visible interfering tiers, as indicated in Eq. (15), thereby increasing aggregate interference. Conversely, increasing the inter-node distance d enlarges the separation between nodes, which increases all UE-to-node distances and reduces interference. In particular, when d becomes sufficiently large (e.g., $d > 2h\tan(\theta_r)$ similar to Eq. (11)), the contribution of interfering nodes becomes negligible and the system approaches an SNR-limited regime. However, the impact of d is not uniform across the cell. Interference reduction occurs more rapidly in the cell-centre region, where UEs are farther from interferers, while cell-edge regions experience a slower reduction due to their proximity to neighbouring nodes. This explains the persistent performance degradation at cell edges and highlights the importance of carefully selecting d (or equivalently node density) to balance interference mitigation, coverage, and spectral efficiency in practical OWC system design.

B. Network Mid Zone

This zone includes all nodes located within a distance w_m from the last row of nodes, as illustrated in Fig. 2. The interference in this zone exhibits a distribution similar to that in the core zone. However, the key difference lies in the reduced number of potential interfering nodes due to the proximity to the system boundary. Unlike the core zone, the mid zone is not symmetric, as the set of potential interfering nodes varies with the UE location and direction relative to the boundary. As a result, the interference characteristics depend on the UE position within this zone. The expected interference in the mid zone is derived in Theorem 3.

Theorem 3: The expected interference experienced by UE when located in the mid zone can be expressed by:

$$\mathbb{E}[I^m] = \int_{\mathbb{D}_c^m} I_c^m(r,h,\alpha)\; f_c^m(r,h,\alpha)\, d\mathbb{D}_c^m + \int_{\mathbb{D}_e^m} I_e^m(r,h,\alpha)\; f_e^m(r,h,\alpha)\, d\mathbb{D}_e^m \tag{19}$$

where $\mathbb{D}_c^m = \mathbb{D}_c^c$ and $\mathbb{D}_e^m = \mathbb{D}_e^c$ denote the bounded spatial domains of the cell-centre and cell-edge regions in the mid zone, respectively, as defined in Theorems 1 and 2. The terms $I_c^m(r,h,\alpha)$ and $I_e^m(r,h,\alpha)$ denote the analytical expressions of the interference in the cell-centre and cell-edge regions of the mid zone, respectively. It is noted that $I_c^m(r,h,\alpha) = I_e^m(r,h,\alpha)$ reflects the identical analytical structure and set of potential interfering nodes in both regions. However, the actual interference values may differ due to variations in the distance-dependent parameters and their corresponding distributions.

$$I_c^m(r,h,\alpha) = \frac{1}{2T-1}\left(\sum_{i=1}^{T} I^c_{c/N_{:,\Phi 1}}(r,h,\alpha) + \sum_{m=2}^{T} I^c_{c/N_{:,\Phi 2}}(r,h,\alpha)\right). \tag{20}$$

where $\frac{1}{2T-1}$ is the likelihood UE being in any half of the cells in the mid zone, $I^c_{c/N_{:,\Phi}}$ denotes the interference in the core zone excluding the nodes located in the angle of Φ, I_c^c is obtained in Theorem 1, $\Phi 1 \in \left[\frac{\pi}{2} + \tan^{-1}\left(\frac{i}{T}\right), \frac{3\pi}{2} - \tan^{-1}\left(\frac{i}{T}\right)\right]$, and $\Phi 2 \in \left[-\tan^{-1}\left(\frac{m}{T}\right), \tan^{-1}\left(\frac{m}{T}\right)\right]$. $f_c^m(r,h,\alpha)$ and $f_e^m(r,h,\alpha)$ denote the joint densities of the random variables r_0, h, and α, whose supports correspond to the cell-centre and cell-edge regions, respectively. Specifically, $f_c^m(r,h,\alpha) = f_c^c(r,h,\alpha)$, as obtained in Theorem 1, and $f_e^m(r,h,\alpha) = f_e^c(r,h,\alpha)$, as obtained in Theorem 2.

Proof: See Appendix C ■

The results in Theorem 3 indicate that the system behaviour in the mid zone is broadly similar to that in the core zone, as the underlying cell geometry and distance parameter distributions remain unchanged due to the identical cell layout and dimensions. However, unlike the core zone, the

mid zone is partially affected by the system boundaries, which reduce the number of active interfering nodes and consequently lower the experienced interference. This effect becomes more pronounced for cells located closer to the system boundary. For example, when the number of interfering tiers is two (e.g., $T = 2$), Eq. (20) shows that the interference term $I^{c}_{c/N_{:,\Phi_1}}(r, h, \alpha)$ when $i = 1$ (the closest nodes of mid zone to the system boundary) excludes nodes within the angular range $\Phi_1 \in \left[\frac{\pi}{2} + \tan^{-1}\left(\frac{1}{2}\right), \frac{3\pi}{2} - \tan^{-1}\left(\frac{1}{2}\right)\right]$ due to the system boundary. As a result, the number of interfering nodes is reduced (e.g., from 24 in the core zone to 14 in this scenario), leading to lower aggregate interference. The number of excluded nodes decreases as the cell moves away from the boundary and towards the core zone, gradually recovering the full interference structure. Consequently, the expected system performance in the mid zone is generally slightly better than that in the core zone. Furthermore, key parameters such as the inter-node distance d exhibit similar trends as in the core zone, although the rate of change differs due to the asymmetry introduced by the system boundary.

C. Network Boundary Zone

The results in Theorems 1 and 2 are derived under the assumption that the cell of interest is surrounded by neighbouring cells in all directions and that the distances between UE and different cells are identical. However, this assumption no longer holds when the cell of interest is located at the system boundary. In this case, no interferers are present beyond the boundary, which reduces the number of interfering nodes and alters the distribution of angular parameters such as α. In addition, the distance between the cell and the system boundary, denoted by $\acute{d}$, can vary independently of the inter-node distance d, leading to further geometric variations. These factors result in different statistical behaviours of location-dependent parameters such as r_0 and α, and therefore the assumptions used in Theorems 1 and 2 are no longer directly applicable in the boundary zone. To provide a clearer geometric interpretation, the boundary cell is classified based on the relative value of $\acute{d}$ with respect to $d/2$. Specifically, when $\acute{d} = d/2$, the cell can be divided into two regions (centre and edge), similar to the core-zone analysis but with modified angular constraints. When $\acute{d} \neq d/2$, the cell is partitioned into three regions (centre, middle, and edge), where both the radial distance r_0 and angular parameter α follow different bounds in each region due to the presence of the system boundary. This classification enables a more accurate representation of practical OWC deployments while explicitly capturing boundary effects. A detailed mathematical formulation of these regions is provided in Theorem 4.

Theorem 4: The expected interference experienced by UE in the boundary zone when $\acute{d} < \frac{d}{2}$ can be expressed by:

$$\begin{aligned}\mathbb{E}[I^b] = &\int_{\mathbb{D}^b_c} I^b_c(r,h,\alpha)\ f^b_c(r,h,\alpha)\, d\mathbb{D}^b_c + \\ &\int_{\mathbb{D}^b_m} I^b_m(r,h,\alpha)\ f^b_m(r,h,\alpha)\, d\mathbb{D}^m_b + \\ &\int_{\mathbb{D}^b_e} I^b_e(r,h,\alpha)\ f^b_e(r,h,\alpha)\, d\mathbb{D}^b_e\end{aligned} \tag{21}$$

where $\mathbb{D}^b_c$, $\mathbb{D}^b_m$, and $\mathbb{D}^b_e$ are the bounded spatial domains of the cell centre, middle, and edge in the boundary zone, respectively, and $I^b_c(r,h,\alpha)$, $I^b_m(r,h,\alpha)$, and $I^b_e(r,h,\alpha)$ denote the corresponding analytical expressions of the interference in these regions. It is important to note that $I^b_c(r,h,\alpha) = I^b_m(r,h,\alpha) = I^b_e(r,h,\alpha)$ refers to the analytical form of the interference expression and the set of potential interfering nodes, which are identical across these regions. However, the actual interference experienced by UE varies spatially due to differences in the distance-dependent parameters r_0, h, and α, as well as the spatial weighting introduced by the corresponding joint densities. The expressions are obtained as follows:

$$I^b_c(r,h,\alpha) = I^c_{c/N_{:,\Phi}:\frac{\pi}{2}>\Phi>\frac{3\pi}{2}}(r,h,\alpha) \tag{22}$$

$I^c_{c/N_{:,\Phi}}(r,h,\alpha)$ denotes the interference in the core area excluding the nodes located in the angular angle of Φ, and $I^c_c(r,h,\alpha)$ is obtained in Theorem 1. Given that UE is located in the boundary zone, the joint densities of the random variables, whose supports correspond to the centre, middle, and edge regions of the cell, are expressed as:

$$f^b_{c,m,e}(r,\alpha,h) = \begin{cases} \frac{2r}{dh_c\acute{d}} & \mathfrak{c} \\ f^b_m(r)\ f^b_m(\alpha|r)\ f^b_m(h) & \mathfrak{m} \\ f^b_e(r)\ f^b_e(\alpha|r)\ f^b_e(h) & \mathfrak{e} \end{cases} \tag{23}$$

where $\frac{2r}{dh_c\acute{d}}$ is the joint density of r_0, α and h in the cell centre, $f^b_m(\alpha|r) = \frac{2}{\pi - 2\cos^{-1}\left(\frac{\acute{d}}{r}\right)}$ is the conditional PDF of α, $f^b_m(r) = \frac{r}{d\acute{d}}\left(\pi - 2\cos^{-1}\left(\frac{\acute{d}}{r}\right)\right)$ is the density of r_0 and $f^b_m(h) = \frac{1}{h_c}$ is the PDF of h in the cell middle. $f^b_e(r) = \frac{2r}{d\acute{d}}\left(\frac{\pi}{2} - \cos^{-1}\left(\frac{\acute{d}}{r}\right) - \cos^{-1}\left(\frac{d}{2r}\right)\right)$ is the density of r_0, $f^b_e(\alpha|r) = \frac{1}{\frac{\pi}{2} - \cos^{-1}\left(\frac{\acute{d}}{r}\right) - \arccos(d/2r)}$ is the PDF of α and $f^b_e(h) = \frac{1}{h_c}$ is the PDF of h in the cell edge. $\mathfrak{c}$ ($\mathbb{D}^b_c$) is the random variables limits in the centre region, $0 \le r_0 \le \acute{d}$, $0 \le \alpha \le \frac{\pi}{2}$ and $h_n - h_c \le h \le h_n$. $\mathfrak{m}$ ($\mathbb{D}^b_m$) is the random variables limits in the middle region, $\acute{d} < r_0 \le \frac{d}{2}$, $0 < \alpha \le \frac{\pi}{2} - \cos^{-1}\left(\frac{\acute{d}}{r}\right)$ and $h_n - h_c \le h \le h_n$. $\mathfrak{e}$ ($\mathbb{D}^b_e$) is the random variables limits in the edge region, $\frac{d}{2} < r_0 \le \sqrt{\acute{d}^2 + d^2/4}$, $\arccos(d/2r) < \alpha \le \frac{\pi}{2} - \cos^{-1}\left(\frac{\acute{d}}{r}\right)$ and $h_n - h_c \le h \le h_n$.

Proof: See Appendix D ■

The results in Theorem 4 are when $\acute{d} < \frac{d}{2}$, in fact $\acute{d}$ can take any value depending on number of system parameters such as the system area, value of d and the number of nodes

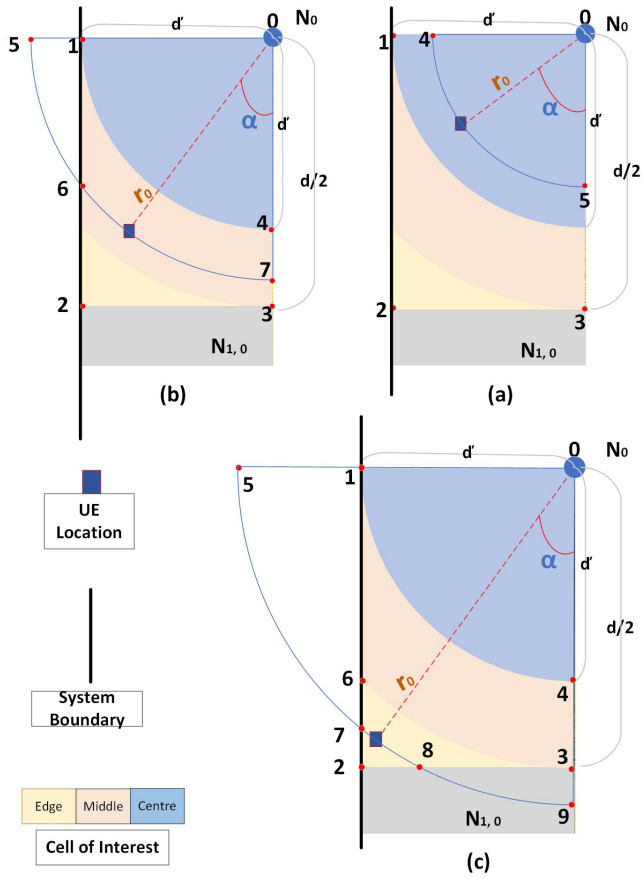

FIGURE 6. **Boundary zone - (a) cell centre, (b) cell middle and (c) cell edge.**

installed in the system. Therefore, the other scenarios need to be considered such as $\acute{d} > \frac{d}{2}$ and $\acute{d} = \frac{d}{2}$. When $\acute{d} > \frac{d}{2}$, the joint density $f^b_{c,m,e}(r, \alpha, h)$ is obtained similar to Theorem 4 and by rewriting Eq. (23):

$$f^b_{c,m,e}(r,\alpha,h) = \begin{cases} \frac{2r}{dh_c\acute{d}} & \mathfrak{c} \\ f^b_m(r)\ f^b_m(\alpha|r)\ f^b_m(h) & \mathfrak{m} \\ f^b_e(r)\ f^b_e(\alpha|r)\ f^b_e(h) & \mathfrak{e} \end{cases} \tag{24}$$

where $\frac{2r}{dh_c\acute{d}}$ is the joint density of r_0, α and h in the cell centre, $f^b_m(\alpha|r) = \frac{2}{\pi - 2\cos^{-1}\left(\frac{d}{2r}\right)}$ is the conditional PDF of α, $f^b_m(r) = \frac{r}{d\acute{d}}\left(\pi - 2\cos^{-1}\left(\frac{d}{2r}\right)\right)$ is the density of r_0 and $f^b_m(h) = \frac{1}{h_c}$ is the PDF of h in the cell middle. $f^b_e(r) = \frac{2r}{d\acute{d}}\left(\frac{\pi}{2} - \cos^{-1}\left(\frac{d}{2r}\right) - \cos^{-1}\left(\frac{\acute{d}}{r}\right)\right)$ is the density of r_0, $f^b_e(\alpha|r) = \frac{1}{\alpha^b_{maxe} - \alpha^b_{mine}}$ is the PDF of α, $\alpha^b_{mine} = \arccos(d/2r)$, $\alpha^b_{maxe} = \frac{\pi}{2} - \cos^{-1}\left(\frac{d}{2r}\right)$ and $f^b_e(h) = \frac{1}{h_c}$ is the PDF of h in the cell edge. $\mathfrak{c}$ is the random variables limits in the centre region, $0 \le r_0 \le \frac{d}{2}$, $0 \le \alpha \le \frac{\pi}{2}$ and $h_n - h_c \le h \le h_n$. $\mathfrak{m}$ is the random variables limits in the middle region, $\frac{d}{2} < r_0 \le \acute{d}$, $0 < \alpha \le \frac{\pi}{2} - \cos^{-1}\left(\frac{d}{2r}\right)$ and $h_n - h_c \le h \le h_n$. $\mathfrak{e}$ is the random variables limits in the edge region, $\acute{d} < r_0 \le \sqrt{\acute{d}^2 + d^2/4}$, $\arccos(\acute{d}/r) < \alpha \le \frac{\pi}{2} - \cos^{-1}\left(\frac{d}{2r}\right)$ and $h_n - h_c \le h \le h_n$.

When $\acute{d} = \frac{d}{2}$, the middle area disappears and the joint densities in Eq. (23): becomes:

$$f^b_{c,e}(r,\alpha,h) = \begin{cases} \frac{\pi r}{\acute{d}^2} & \mathfrak{c} \\ f^b_e(r)\ f^b_e(\alpha|r)\ f^b_e(h) & \mathfrak{e} \end{cases} \tag{25}$$

where $\frac{\pi r}{\acute{d}^2}$ is the joint density of r_0, α and h in the cell centre, $f^b_e(r) = \frac{r}{\acute{d}^2}\left(\frac{\pi}{2} - \cos^{-1}\left(\frac{\acute{d}}{r}\right)\right)$ is the density of r_0, $f^b_e(\alpha|r) = \frac{1}{\frac{\pi}{2} - \arccos(\acute{d}/r)}$ is the PDF of α, and $f^b_e(h) = \frac{1}{h_c}$ is the PDF of h in the cell edge. $\mathfrak{c}$ is the random variables limits in the centre region, $0 \le r_0 \le \acute{d}$, $0 \le \alpha \le \frac{\pi}{2}$ and $h_n - h_c \le h \le h_n$. $\mathfrak{e}$ is the random variables limits in the edge region, $\acute{d} < r_0 \le \acute{d}\sqrt{2}$, $\arccos(\acute{d}/r) < \alpha \le \frac{\pi}{2}$ and $h_n - h_c \le h \le h_n$.

The results in Theorem 4 further highlight the impact of system boundaries on interference behaviour. In addition to the reduction in the number of interfering nodes, the distributions of the distance-dependent parameters, e.g. r_0 and α, are strongly influenced by the proximity to the system boundary. In particular, the maximum distance to the nearest interferer increases to $\sqrt{d^2 + \acute{d}^2}$ in the boundary zone, compared to d in the core and mid zones. This is a direct consequence of the absence of nodes beyond the system boundary. Moreover, the geometric constraints imposed by the boundary introduce additional complexity in modelling the distributions of the distance parameters, requiring partitioning of the cell into multiple regions. Due to the combined effects of reduced interference and increased separation from interfering nodes, the boundary zone can exhibit improved performance compared to other regions. These observations emphasise the importance of explicitly accounting for boundary effects in the analysis of finite OWC networks.

D. Higher Reuse Factor

The results in the previous subsections are derived under the assumption of a reuse factor of one, whereby the available bandwidth is reused by all nodes in the system. However, this assumption is not always valid in practical deployments, where higher reuse factors are often adopted to mitigate interference and improve overall performance [32]. Increasing the reuse factor enlarges the minimum distance between co-channel cells, thereby reducing mutual interference. In the following, the proposed framework is extended to incorporate resource reuse. In particular, a reuse factor of three is considered in Theorem 5 to illustrate how the framework captures changes in the interference structure and to evaluate the resulting performance improvements in finite networks.

Theorem 5: The expected interference experienced by UE in the core, mid and boundary zones when the reuse factor

is 3 can be expressed by:

$$\mathbb{E}[I^{z3}] = \int_{\mathbb{D}_c^{z3}} I_c^{z3}(r,h,\alpha)\ f_c^{z3}(r,h,\alpha)\, d\mathbb{D}_c^{z3} + \Gamma(\acute{d}) \int_{\mathbb{D}_m^{z3}} I_m^{z3}(r,h,\alpha)\ f_m^{z3}(r,h,\alpha)\, d\mathbb{D}_{z3}^{m} + \int_{\mathbb{D}_e^{z3}} I_e^{z3}(r,h,\alpha)\ f_e^{z3}(r,h,\alpha)\, d\mathbb{D}_e^{z3} \tag{26}$$

where $z \in \{c,m,b\}$, $\mathbb{D}_c^{z3} = \mathbb{D}_c^z$, $\mathbb{D}_m^{z3} = \mathbb{D}_m^z$ and $\mathbb{D}_e^{z3} = \mathbb{D}_e^z$ are the bounded spatial domain of the cell centre, middle and edge in zth zone obtained in Theorem 1, 2 and 4 respectively, and $\Gamma(\acute{d})$ is expressed by:

$$\Gamma(\acute{d}) = \begin{cases} 1 & z = b\ \&\ \acute{d} \neq \frac{d}{2} \\ 0 & \text{otherwise} \end{cases} \tag{27}$$

$f_c^{z3}(r,h,\alpha) = f_c^z(r,h,\alpha)$, $f_m^{z3}(r,h,\alpha) = f_m^z(r,h,\alpha)$, and $f_e^{z3}(r,h,\alpha) = f_e^z(r,h,\alpha)$ are the joint densities in different areas of the cell in zth zone obtained in Theorem 1, 2 and 4. $I_c^{z3}(r,h,\alpha)$, $I_m^{z3}(r,h,\alpha)$, and $I_e^{z3}(r,h,\alpha)$ denote the analytical expressions of the interference in the cell-centre, middle, and edge regions of the zth zone, respectively.

$$I_a^{c3}(r,h,\alpha) = I_{a(\acute{T}-2)}^{c3} + Kh^{\mu+1} \sum_{i=1}^{4} \left(C_{\acute{T},\Psi_{i1}}^c + C_{\acute{T},\Psi_{i2}}^c\right) + \sum_{t=2,4,\cdots}^{\acute{T}-2} \sum_{m=1}^{4} \left(C_{\acute{T},\Psi_{tm1}}^c + C_{\acute{T},\Psi_{tm2}}^c\right) \tag{28}$$

$$I_a^{m3}(r,h,\alpha) = \frac{1}{2T-1} \left(\sum_{i=1}^{T} I_{a/N_{:,\Phi 1}}^{c3} + \sum_{m=2}^{T} I_{a/N_{:,\Phi 2}}^{c3} \right) \tag{29}$$

$$I_a^{b3}(r,h,\alpha) = I_{a/N_{:,\Phi}:\frac{\pi}{2}>\Phi>\frac{3\pi}{2}}^{c3} \tag{30}$$

where $C_{\acute{T},\Psi_{i1}}^c = \left(r_{\acute{T},\Psi_{i1}}^2 + h^2\right)^{-\frac{\mu+3}{2}} \Gamma(r_{\acute{T},\Psi_{i1}})$, $C_{\acute{T},\Psi_{i2}}^c = \left(r_{\acute{T},\Psi_{i2}}^2 + h^2\right)^{-\frac{\mu+3}{2}} \Gamma(r_{\acute{T},\Psi_{i2}})$, $C_{\acute{T},\Psi_{tm1}}^c = \left(r_{\acute{T},\Psi_{tm1}}^2 + h^2\right)^{-\frac{\mu+3}{2}} \Gamma(r_{\acute{T},\Psi_{tm1}})$ and $C_{\acute{T},\Psi_{tm2}}^c = \left(r_{\acute{T},\Psi_{tm2}}^2 + h^2\right)^{-\frac{\mu+3}{2}} \Gamma(r_{\acute{T},\Psi_{tm2}})$. The corresponding values of $r_{\acute{T},\Psi_\star}$ and $\Psi_\star$ are obtained as in Theorem 1. $\Phi 1 \in \left[\frac{\pi}{2} + \tan^{-1}\left(\frac{i}{T}\right), \frac{3\pi}{2} - \tan^{-1}\left(\frac{i}{T}\right)\right]$, $\Phi 2 \in \left[-\tan^{-1}\left(\frac{m}{T}\right), \tan^{-1}\left(\frac{m}{T}\right)\right]$ and $a \in \{c,m,e\}$ is the area in the cell. $I_{c/N_{:,\Phi}:\frac{\pi}{2}>\Phi>\frac{3\pi}{2}}^{c3}$, $I_{a/N_{:,\Phi 1}}^{c3}$ and $I_{a/N_{:,\Phi 2}}^{c3}$ denotes the interference in the core area obtained in Eq.(28) excluding the nodes located in the angle of Φ, $\Phi 1$ and $\Phi 2$ respectively.

Proof: See Appendix E ■

Although a reuse factor of 3 is considered in this work as a representative case, the proposed framework is general and can be systematically extended to arbitrary reuse factors. Specifically, this extension can be achieved by: (i) redefining the set of co-channel interfering nodes according to the adopted reuse pattern, (ii) updating the corresponding tier structure and inter-node distances to reflect the increased separation between active cells, and (iii) evaluating the resulting interference using the same probabilistic framework for UE location and distance distributions. The coverage probability is then obtained by integrating the modified interference expressions over the corresponding spatial domains, following the same procedure described in this work. In general, increasing the reuse factor enlarges the minimum distance between co-channel cells and reduces the number of active interfering nodes, thereby lowering interference levels and improving coverage probability. However, this improvement comes at the expense of reduced spectral efficiency, as the available resources are reused less frequently across the network. In addition, practical constraints such as the FOV and the inter-node distance limit the range of feasible reuse factors. For sufficiently large reuse factors, the system behaviour may approach an SNR-limited regime, reducing the benefits of resource reuse. Overall, the proposed analytical framework provides a flexible tool for evaluating different reuse configurations by appropriately modifying the set of interfering nodes, the number of contributing tiers, and the associated geometric constraints, enabling systematic analysis of reuse strategies and their trade-offs in practical OWC network design.

It is important to note that, under higher reuse factors, the geometric structure of the system remains unchanged. In particular, the impact of system and cell boundaries, as well as the distributions of the distance-dependent parameters r_0, α, and h, remain identical to those derived for the reuse factor of 1. The key difference lies in the reduced number of co-channel interfering nodes, as only a subset of nodes remains active. Consequently, the interference expressions retain the same analytical form, while the summation over interfering nodes is performed over a reduced set. This leads to lower aggregate interference and improved coverage performance, without altering the underlying spatial distributions.

IV. Coverage Probability

In a finite downlink OWC system, the coverage probability is defined as the probability that the received SINR at a given UE location exceeds a predefined threshold γ. Mathematically, this can be expressed as:

$$\mathcal{CP} = \mathcal{CP}^c + \mathcal{CP}^m + \mathcal{CP}^b \tag{31}$$

where $\mathcal{CP}^c$, $\mathcal{CP}^m$ and $\mathcal{CP}^b$ are the coverage probability in each zone of the system, core, mid and boundary respectively. The coverage probability in zth zone is obtained by:

$$\begin{aligned} \mathcal{CP}^z(\gamma) &= \mathcal{P}^z \mathbb{P}[SINR^z > \gamma] \\ &= \mathcal{P}^z \int_{\mathbb{D}^z} \mathbb{P}\Big[SINR^z(r,h,\theta) > \gamma\Big]\ f^z(r,h,\theta)\ d\mathbb{D}^z \\ &= \mathcal{P}^z \int_{\mathbb{D}^z} \mathbb{P}\Big[\frac{S^z(r,h)}{I^z(r,h,\theta)+\sigma^2} > \gamma\Big]\ f^z(r,h,\theta)\ d\mathbb{D}^z \\ &= \mathcal{P}^z \int_{\mathbb{D}^z} 1\Big(S^z(r,h) > \gamma\big(I^z(r,h,\theta)+\sigma^2\big)\Big) \\ &\qquad f^z(r,h,\theta)\ d\mathbb{D}^z \end{aligned} \tag{32}$$

where $z \in \{c, m, b\}$, $SINR^z(r, h, \theta)$ is the SINR experienced by UE in zth zone, γ is the SINR threshold, $\mathbb{D}^z$ is the bounded spatial domain of zth zone, $f^z(r, h, \theta)$ is the joint PDF distribution of location parameters in zth zone, $S^z(r, h) = Kh^{\mu+1}(r^2 + h^2)^{-\frac{\mu+3}{2}}$, I^z is the interference experienced by UE when it is located in zth zone, $\sigma^2 = \eta BW$ denotes the noise variance, η is the noise power spectral density, and BW is the system bandwidth. Note that I^z, $f^z(r, h, \theta)$ and $\mathbb{D}^z$ are obtained in Theorem 1 and 2 when $z = c$, Theorem 3 when $z = m$ and Theorem 4 when $z = b$. Furthermore, finding the coverage probability for higher reuse factor (e.g. 3), the aforementioned parameters are obtained in Theorem 5.

V. Results

The results in this section demonstrate the accuracy of the proposed analysis and illustrate the impact of key system parameters and environmental characteristics. MATLAB is used to simulate the interference and coverage probability in a finite regular network with dimensions l_s and w_s. The simulation results are obtained by averaging over 10^6 Monte Carlo realizations, where UEs are randomly distributed within the system area. The environment is assumed to be covered by a grid of regularly shaped (square) cells, as shown in Fig. 2. Nodes are placed at the centres of the cells at a height of h_n from the floor, and the inter-node distance is set to d. For each realization, the UE location is randomly generated within the system, and the distances between UE and all nodes are computed accordingly. The serving node is identified as the closest node. The channel gain to the serving node is obtained according to Eq. (3), while the gains to the remaining nodes are calculated using Eq. (10), accounting for the UE location and its distances to all interfering nodes. The resulting interference and coverage probability are then evaluated, and the simulation results are denoted by Sim. Unless otherwise specified, the system parameters used in the simulations are listed in Table 2. The parameter values listed in Table 2 are selected based on commonly adopted settings in the OWC literature and representative practical deployment scenarios, ensuring realistic and reproducible performance evaluation (see, e.g., [2], [33]).

The semi-analytical expressions are evaluated numerically using MATLAB. The agreement between the analytical and simulation results is assessed through direct comparison of the corresponding curves.

Fig. 7 shows the expected interference experienced by UE for different values of the inter-node distance (d). In this figure, BZ-Num and BZ-Sim, MZ-Num and MZ-Sim, and CZ-Num and CZ-Sim denote the numerical and simulation results for the boundary, mid, and core zones, respectively, while DA represents the conventional disc-assumption model. The results clearly demonstrate that the expected interference decreases as d increases. This behaviour is due to two factors: (i) the reduction in the number of active interfering nodes, and (ii) the increased distance

TABLE 2. System Parameters

Symbol	Name	Value
η	Noise power spectral density	$10^{-20}A^2/Hz$
BW	Bandwidth	20 MHz
θ	Semi-angle at half power	70°
P_t	Transmitted optical power	2 W
A_{det}	Detector physical area	$10^{-4}m^2$
T_s	Gain of optical filter	1
G_{con}	Gain of optical concentrator	1
h	Height difference	3 m
d	Node inter-distance	2 m
$\acute{d}$	Last row-system boundary distance	1m
l_s	System length	100 m
w_s	System width	50 m

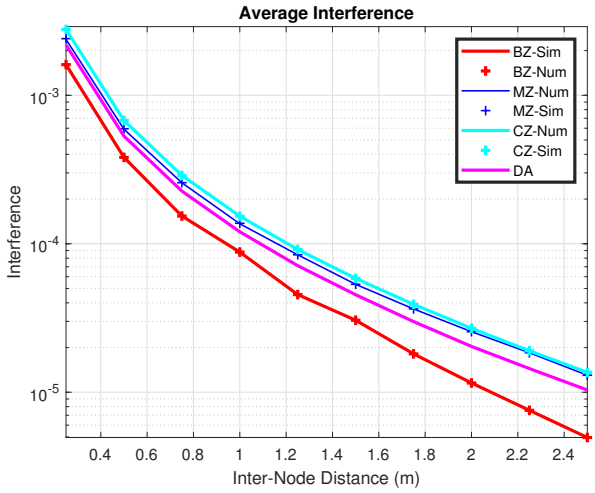

FIGURE 7. Interference vs in different system zones. CZ, MZ, and BZ denote the interference in the core, mid, and boundary zones, respectively. Num and Sim represent the numerical results obtained using the proposed analytical framework and the simulation results, respectively. DA corresponds to the interference obtained under the commonly adopted disc-assumption model in the literature.

between UE and the interferers, both of which reduce the aggregate interference power. A key observation from Fig. 7 is the discrepancy between the proposed model and the DA model. While the simulation results closely match the analytical results, validating the accuracy of the proposed framework, the DA model consistently underestimates the interference. This is because it neglects contributions from cell-edge regions and does not accurately capture the spatial variability of interference within the cell. Furthermore, the figure highlights the impact of the UE location within the network. The interference is highest in the core zone, where UE is surrounded by interferers in all directions, and de-

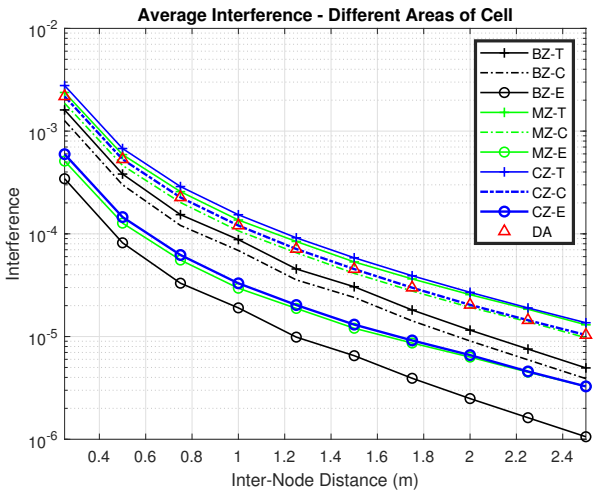

FIGURE 8. Average interference in centre and edge regions of cells versus inter-node distance. Results are shown for the core, mid, and boundary zones, and the limitations of the disc-assumption (DA) model.

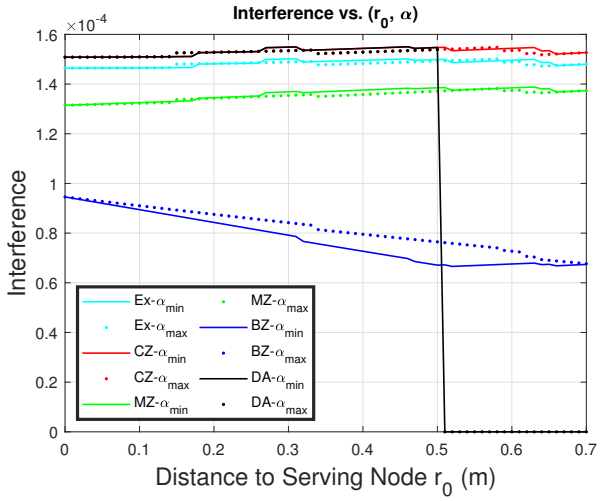

FIGURE 9. Interference versus distance to the serving node for different zones and angular positions. Results are shown for the core, mid, and boundary zones, including the expected-interference (Ex) and disc-assumption (DA) models.

creases progressively in the mid and boundary zones. In the boundary zone, the interference reaches its lowest values due to the absence of interfering nodes beyond the system edge. This trend clearly demonstrates the importance of accounting for finite network geometry and boundary effects in practical OWC system analysis.

Unlike Fig. 7, Fig. 8 illustrates the average interference experienced by UE within different areas of a cell (centre and edge) for various inter-node distances (d). In this figure, both regions are evaluated across all system zones. Specifically, CZ-T, MZ-T, and BZ-T denote the total interference in the core, mid, and boundary zones, respectively, while CZ-C, MZ-C, and BZ-C correspond to the average interference in the cell-centre regions, and CZ-E, MZ-E, and BZ-E represent the average interference in the cell-edge regions. By definition, $(CZ\text{-T}) = (CZ\text{-C}) + (CZ\text{-E})$, $(MZ\text{-T}) = (MZ\text{-C}) + (MZ\text{-E})$, and $(BZ\text{-T}) = (BZ\text{-C}) + (BZ\text{-E})$. The results show that increasing d reduces the interference across all regions and zones. This reduction is driven by both the decreasing density of interfering nodes and the increased separation between UE and interferers. A key observation is that the cell-edge regions consistently experience higher interference than the cell-centre regions, particularly in the core zone. This is because UEs located near the cell edge are closer to neighbouring nodes, leading to stronger interference contributions. In contrast, this effect is less pronounced in the mid and boundary zones, where the number of active interferers is reduced due to the presence of the system boundary. The figure also highlights the limitations of the disc-assumption (DA) model. The DA results closely match the interference levels in the cell-centre region of the core zone (CZ-C), indicating that this model effectively captures only the centre region while neglecting the edge regions, where interference is significantly higher and performance degradation is most severe. Finally, the rate of interference reduction with increasing d differs across zones. The reduction is more pronounced in the core zone, where interferers surround UE in all directions, compared to the mid and boundary zones, where interference is inherently limited by the system boundary. As a result, the difference in interference levels between zones decreases as d increases.

Fig. 9 illustrates the interference experienced by UE as a function of its distance from the serving node, denoted by r_0. Different system zones are considered, where CZ, MZ, and BZ correspond to the core, mid, and boundary zones, respectively. The curve Ex represents the expected interference for a randomly located UE, while DA denotes the disc-assumption model. In addition, two angular extremes, $\alpha_{\min}$ and $\alpha_{\max}$, are evaluated for each scenario. These values depend on the cell region; for example, in the core zone, $\alpha_{\min} = 0$ and $\alpha_{\max} = \pi/4$ in the centre region, while $\alpha_{\min} = \cos^{-1}\left(\frac{d}{2r}\right)$ and $\alpha_{\max} = \pi/4$ in the edge region. A key observation is that interference is generally highest at the cell-edge regions, particularly in the core and mid zones. This highlights the limitation of the disc-assumption (DA) model, which considers only the cell-centre region. Under the DA assumption, the interference drops to zero when $r_0 > d/2$, which is inconsistent with the other scenarios. In practice, UEs experience non-zero interference across both centre and edge regions, as captured by the proposed model. The figure also shows that, in the core and mid zones, the interference increases as UE moves away from the serving node. This occurs because UE approaches neighbouring interferers even as it moves farther from others, leading to an overall increase in aggregate interference. In contrast, in the boundary zone, the interference decreases with increasing r_0. This is because UE moves closer to the system boundary and farther from all interfering nodes, resulting in reduced interference. Another important observation is the impact

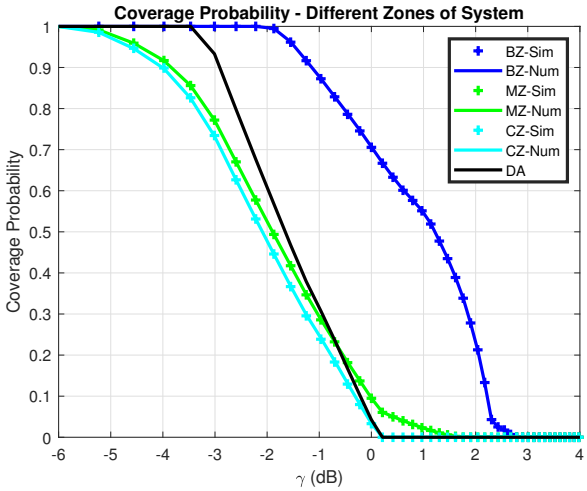

FIGURE 10. **Coverage probability versus SINR threshold. Results are shown for the core, mid, and boundary zones, including numerical (Num) and simulation (Sim) results, together with the disc-assumption (DA) model.**

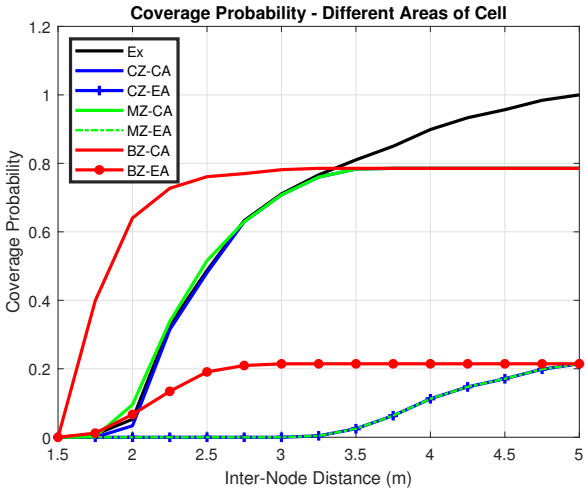

FIGURE 11. **Coverage probability versus inter-node distance. Results are shown for centre and edge regions of cells in the core, mid, and boundary zones.**

of the angular position α. In the core and mid zones, the interference is generally maximized at $\alpha_{\min}$, reflecting the geometric alignment with nearby interferers. However, in the boundary zone, where the interference environment is asymmetric, the opposite behaviour is observed: $\alpha_{\max}$ corresponds to higher interference, as UE becomes closer to one of the neighbouring interferers, while $\alpha_{\min}$ corresponds to the lowest interference.

Finally, the expected interference (Ex) is slightly lower than that in the core zone for all values of r_0. This is because, although interference levels in the mid and boundary zones are smaller, the overall expectation is dominated by the core zone due to its larger spatial extent. The relative contributions of different zones depend on system parameters such as inter-node distance (d), transmitter–receiver height difference, field of view (FOV), and system dimensions.

Fig. 10 presents the coverage probability of the OWC system as a function of the SINR threshold. Simulation results are included to validate the analytical model. In this figure, CZ, MZ, and BZ denote the coverage probabilities in the core, mid, and boundary zones, respectively; Sim and Num represent simulation and analytical results; and DA corresponds to the conventional disc-assumption model. The results demonstrate excellent agreement between the analytical and simulation curves, confirming the accuracy of the proposed framework. As expected, the coverage probability decreases with increasing SINR threshold, since stricter SINR requirements reduce the spatial regions within each cell that satisfy the threshold. A key observation is the significant discrepancy between the proposed model and the DA model. The DA model substantially overestimates system performance, particularly at moderate SINR thresholds. For example, at an SINR threshold of -3 dB, the DA model predicts approximately 95% coverage, whereas the proposed model and simulations indicate that only about 75% of the core and mid zones satisfy this threshold. This discrepancy arises because the DA model neglects the cell-edge regions, where UEs experience both reduced desired signal power and increased interference. The figure also reveals that the performance gap between the DA and CZ results is more pronounced at low SINR thresholds. In this regime, the coverage probability reflects contributions from the entire cell, including low-performance edge regions. As the SINR threshold increases, these edge regions are progressively excluded, and the CZ results become dominated by the cell-centre regions, leading to closer agreement with the DA model. Furthermore, the results highlight the strong spatial dependence of coverage across different zones. The core zone exhibits the lowest coverage probability due to the presence of interferers in all directions. The mid zone provides intermediate performance, while the boundary zone achieves the highest coverage probability, benefiting from the reduced number of interfering nodes near the system boundary.

Overall, these results demonstrate that accurate modelling of spatial variability and boundary effects is essential for reliable performance evaluation and practical OWC network design.

Fig. 11 illustrates the coverage probability in different cell areas for various system zones and inter-node distances (d). As expected, the overall system performance improves with increasing d. This is because larger inter-node distances increase the separation between UE and interfering nodes, while also reducing the total number of active interferers, leading to higher SINR levels. A key observation is that the boundary zone consistently achieves the highest coverage probability across all values of d. This is due to the reduced number of interfering nodes near the system boundary. It can be observed that both the centre and edge regions of the

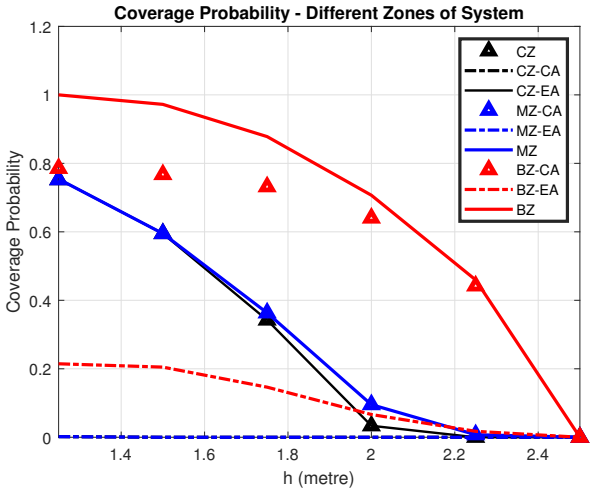

FIGURE 12. Coverage probability versus height difference. Results are shown for centre and edge regions of cells in the core, mid, and boundary zones at an SINR threshold of 0 dB.

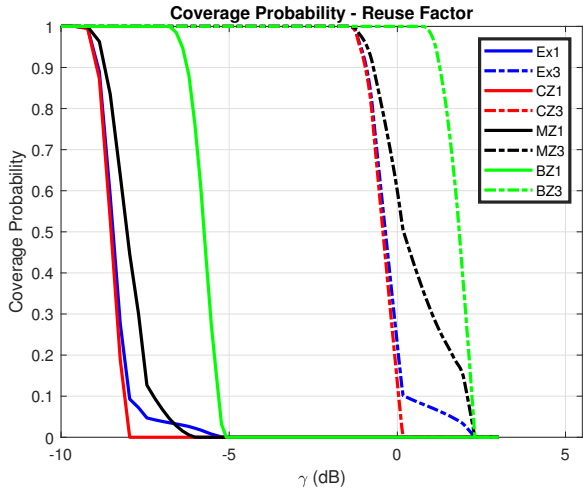

FIGURE 13. Coverage probability versus SINR threshold under different reuse factors. Results are shown for the core, mid, and boundary zones with reuse factors 1 and 3.

boundary cells reach near-perfect coverage when $d \approx 2.5$ m, i.e., $BZ\text{-}CA + BZ\text{-}EA \approx 1$. However, despite this high performance, the boundary zone has a limited impact on the overall system performance (Ex) because it occupies a relatively small portion of the total system area. This highlights the importance of spatial weighting when evaluating overall performance. In contrast, the centre regions of the core and mid zones ($CZ\text{-}CA$ and $MZ\text{-}CA$) exhibit degraded performance at small inter-node distances ($d < 2$ m), but improve significantly as d increases, approaching full coverage for $d > 3$ m. The edge regions of these zones ($CZ\text{-}EA$ and $MZ\text{-}EA$), however, experience the lowest coverage, particularly for $d \leq 3$ m, and only begin to improve noticeably for $d \gtrsim 3.5$ m. These results emphasise that the cell-edge regions represent the performance bottleneck of the system. Neglecting these regions, as in conventional disc-assumption models, leads to overly optimistic performance estimates. Therefore, accurate modelling of both spatial variability and cell-edge effects is essential for reliable system design and performance evaluation.

Fig. 12 illustrates the coverage probability across all system zones—core, mid, and boundary—for different UE heights at an SINR threshold of 0 dB. The figure shows the coverage probability for both centre and edge regions within each zone, where $CZ\text{-}CA$, $MZ\text{-}CA$, and $BZ\text{-}CA$ denote the centre regions, and $CZ\text{-}EA$, $MZ\text{-}EA$, and $BZ\text{-}EA$ denote the edge regions. The results clearly demonstrate the significant impact of UE height on system performance. As the height difference h increases, the coverage probability decreases across all zones. This degradation is primarily due to the increase in the number of visible interferers, as larger height differences expand UE's FOV and allow more nodes to contribute to interference. A key observation is that the edge regions experience the most severe performance degradation, particularly in the core and mid zones. In these zones, the coverage in the edge regions ($CZ\text{-}EA$ and $MZ\text{-}EA$) becomes nearly zero for all values of h, resulting in $CZ \approx CZ\text{-}CA$ and $MZ \approx MZ\text{-}CA$. This highlights that system performance in these zones is effectively dominated by the centre regions under increasing interference conditions. The figure also shows that the performance in the core and mid zones is similar for small height differences ($h \leq 1.5$ m). However, for larger values of h, the mid zone outperforms the core zone. This is because, although the number of interferers increases with h in both zones, the rate of increase is lower in the mid zone due to the presence of the system boundary, which limits the number of contributing interferers. The boundary zone consistently achieves the highest coverage probability, as it is affected by the smallest number of interferers. Overall, these results highlight the critical role of UE height and further emphasise that cell-edge regions—particularly in the core and mid zones—are the most vulnerable to performance degradation due to increased interference and reduced received signal strength.

Fig. 13 presents the coverage probability across different system zones for reuse factors of 1 and 3. Specifically, $Ex1$, $CZ1$, $MZ1$, and $BZ1$ denote the overall, core, mid, and boundary zone coverage probabilities, respectively, for a reuse factor of 1, while $Ex3$, $CZ3$, $MZ3$, and $BZ3$ represent the corresponding results for a reuse factor of 3. The results clearly demonstrate that increasing the reuse factor significantly improves system performance across all zones. This improvement arises because a higher reuse factor increases the spatial separation between co-channel cells, thereby reducing the number of active interferers and increasing their distance from UE.

A key observation is that the performance gain is most pronounced in the mid zone, when a higher reuse factor (e.g., 3) is applied. For SINR thresholds above approx-

imately 3 dB, the coverage probability in the mid zone becomes comparable to that of the boundary zone. For lower thresholds, the mid zone still exhibits slightly lower performance, reflecting the spatial variability within this region. In particular, cells closer to the core zone experience higher interference, while those closer to the boundary benefit from reduced interference. In contrast, the improvement in the core zone is less significant. This is because the core zone is symmetrically surrounded by interferers in all directions. As a result, even though some interferers are removed when a higher reuse factor is applied, UE may still remain close to other interferers, leading to a smaller net performance gain. The boundary zone continues to achieve the highest coverage probability due to the inherently limited number of interferers. Overall, these results highlight that the effectiveness of reuse strategies depends strongly on the spatial location within the network, and that the greatest benefits are achieved in regions where interference is already partially constrained by system geometry.

From a system design perspective, the presented results provide several important insights into the impact of key parameters. The inter-node distance d (or equivalently node density) plays a central role in controlling interference, where increasing d reduces both the number of active interferers and their contribution, gradually shifting the system towards an SNR-limited regime. However, excessively large values of d may lead to coverage gaps and reduced spatial reuse, indicating the need for careful selection of node density. The choice of d should therefore consider system requirements alongside other parameters, such as the transmitter–receiver height difference, system dimensions, and vulnerable regions within the network—particularly the core zone and cell-edge areas. Larger height differences were found to degrade performance by increasing the number of visible interferers within the receiver field of view. In addition, the results consistently show that cell-edge regions represent the primary performance bottleneck due to their proximity to neighbouring nodes and increased exposure to interference. This highlights the importance of incorporating targeted mitigation strategies for these regions. Furthermore, increasing the reuse factor effectively reduces interference by limiting the number of co-channel interferers, resulting in improved coverage performance. However, this comes at the expense of reduced spectral efficiency, emphasising the need to balance interference mitigation and resource utilisation. Finally, the results demonstrate that system performance varies significantly across different zones of the network. This spatial variability suggests that adopting zone-specific design strategies—such as varying reuse factors or inter-node spacing—may further improve performance and resource efficiency. Overall, these observations underline the importance of accurately modelling spatial variability to identify optimal system configurations and guide practical OWC network design.

VI. Conclusion

This paper presented a comprehensive analytical framework for evaluating interference and coverage performance in finite OWC networks with regularly deployed nodes. Unlike conventional approaches based on infinite-network or disc-shaped cell assumptions, the proposed framework explicitly accounts for finite system dimensions, three-dimensional distance variations, and boundary effects. The network was classified into core, mid, and boundary zones to capture the spatial variability of interference arising from truncated interferer sets near the system edges. Semi-analytical expressions for the interference distribution were derived for each zone, demonstrating that the number and geometry of interferers vary significantly across the system. The analysis revealed that, although the core and mid zones exhibit similar interference characteristics, the mid zone experiences reduced interference due to boundary constraints. In contrast, the boundary zone exhibits fundamentally different interference behaviour resulting from both the reduced number of interferers and altered geometric distributions of the serving distance and angular position. Furthermore, the results showed that cell-edge regions—particularly in the core and mid zones—experience the most severe performance degradation due to their larger distances from serving nodes and proximity to neighbouring interferers. Simulation results validated the proposed model and highlighted the limitations of the commonly adopted disc-shaped cell assumption. The disc-based model was shown to substantially overestimate system performance by neglecting edge regions and boundary effects, leading to overly optimistic coverage predictions. In contrast, the proposed framework accurately captures spatial variations across the entire system and provides a realistic assessment of interference and coverage performance. The impact of key system parameters was also investigated. Increasing the inter-node distance or adopting higher frequency reuse factors was shown to significantly improve performance by reducing both the number and strength of interfering signals. Conversely, larger transmitter–receiver height differences were found to degrade performance by increasing the number of visible interferers within the receiver field of view. Overall, the proposed framework provides a robust and flexible foundation for analysing finite OWC networks under structured LOS-dominant conditions, enabling more reliable system design, performance optimisation, and interference management.

The results also highlight important implications for practical network planning. In particular, conventional models based on circular-cell approximations tend to overestimate coverage probability, as they do not accurately capture the true geometry and interference characteristics of regularly deployed OWC networks. This overestimation may lead to overly optimistic system design, where node density is underestimated or inter-node spacing is selected suboptimally. Consequently, coverage gaps or performance degradation may arise, particularly in cell-edge regions where inter-

ference and distance variations are more significant. The proposed framework provides a more realistic evaluation of system performance, enabling more accurate design and optimisation of OWC deployments.

Future work will extend this framework to incorporate NLOS reflections, which may be significant in practical indoor environments with reflective surfaces and complex geometries. In addition, blockage effects and transmitter–receiver misalignment will be considered, as they can introduce additional randomness and significantly impact link reliability and system performance in realistic OWC deployments. Furthermore, user mobility, irregular network deployments, and adaptive resource allocation will be investigated, along with hybrid RF/OWC architectures, to enhance the realism and applicability of the proposed model. An important direction for future research is also the optimisation of node density, or equivalently the inter-node distance, using the proposed analytical framework. Such optimisation would enable the identification of deployment configurations that balance system performance and infrastructure cost, thereby providing valuable insights for practical OWC system design.

Appendix A

Since the core area is symmetric and UE is randomly located, the triangular region 012 in Fig. 4 is considered to analyse the interference caused by other nodes. The angle α is defined as the angle between r_0 and the baseline L_0, and it can take values in the range $[0, \frac{\pi}{4}]$. Considering the interference generated by the closest interferer in the first tier, $N_{1,0}$, and experienced by UE located at the cell centre, the interference from $N_{1,0}$, derived from Eq. (10), is expressed as:

$$\begin{aligned} C^c_{1,0} &= G_{1,0}P_t \\ &= Kh^{\mu+1}\left(r^2_{1,0}+h^2\right)^{-\frac{\mu+3}{2}}\Gamma(r_{1,0}) \end{aligned} \tag{33}$$

where P_t is the transmit power, $K = \frac{P_t(\mu+1)A_{det}G_{con}T_s}{2\pi}$, and $r_{1,0} = \sqrt{r_0^2+d^2-2r_0d\cos(\alpha)}$ denote the horizontal distance between UE and $N_{1,0}$, respectively. The parameter r_0 is the horizontal distance between UE and its serving node N_0, taking values in the range $0 \le r_0 \le \frac{d}{2}$ in the cell-centre region, as shown in Fig. 4. The distance between the serving node N_0 and the interferer $N_{1,0}$ is d. When considering the interference caused by the second closest interferer node $N_{1,\frac{\pi}{2}}$, Eq. (33) becomes:

$$C^c_{1,\frac{\pi}{2}} = Kh^{\mu+1}\left(r^2_{1,\frac{\pi}{2}}+h^2\right)^{-\frac{\mu+3}{2}}\Gamma(r_{1,\frac{\pi}{2}}) \tag{34}$$

where $r_{1,\frac{\pi}{2}} = \sqrt{r_0^2+d^2-2r_0d\cos\left(\frac{\pi}{2}-\alpha\right)}$ is horizontal distance between UE and $N_{1,\frac{\pi}{2}}$, and distance between N_0 and $N_{1,\frac{\pi}{2}}$ is also d. If interference is contributed only by the first tier ($T=1$), the maximum number of interferers is 8, located at distinct angular positions (e.g., $0, \frac{\pi}{4}, \frac{\pi}{2}, \ldots, \frac{7\pi}{4}$) with respect to L_0. The analytical expression of the interference in the cell-centre region, $I^c_c(r,h,\alpha)$, caused by these potential 8 interfering nodes is given by:

$$\begin{aligned} I^c_c(r,h,\alpha) &= \sum_{i=1}^{4} C^c_{1,\Psi_{i1}} + C^c_{1,\Psi_{i2}} \\ &= \sum_{i=1}^{4} Kh^{\mu+1}\Big(\left(r^2_{1,\Psi_{i1}}+h^2\right)^{-\frac{\mu+3}{2}}\Gamma(r_{1,\Psi_{i1}}) \\ &\quad + \left(r^2_{1,\Psi_{i2}}+h^2\right)^{-\frac{\mu+3}{2}}\Gamma(r_{1,\Psi_{i2}})\Big) \end{aligned} \tag{35}$$

where $r_{1,\Psi_{i1}} = \sqrt{r_0^2+d^2-2r_0d\cos(\Psi_{i1}-\alpha)}$ and $r_{1,\Psi_{i2}} = \sqrt{r_0^2+2d^2-2\sqrt{2}r_0d\cos(\Psi_{i2}-\alpha)}$ are distances between UE and $N_{1,\Psi_{i1}}$ and $N_{1,\Psi_{i2}}$, respectively, $\Psi_{i1} = \frac{(i-1)\pi}{2}$, and $\Psi_{i2} = \frac{\pi}{4}+\frac{(i-1)\pi}{2}$. If the number of contributing tiers is two ($T=2$), the total number of potential interferers increases to 24 (8 nodes from tier 1 and 16 nodes from tier 2). Accordingly, the analytical expression of the interference in the cell-centre region, $I^c_c(r,h,\alpha)$, becomes:

$$\begin{aligned} I^c_c(r,h,\alpha) = I^c_{c(1)} &+ \sum_{i=1}^{4}\left(C^c_{2,\Psi_{i1}}+C^c_{2,\Psi_{i2}}\right) + \sum_{m=1}^{4}\Big(C^c_{2,\Psi_{m1}} \\ &+ C^c_{2,\Psi_{m2}}\Big) \end{aligned} \tag{36}$$

where $I^c_{c(1)}$ is the interference caused by the first tier and obtained in Eq. (35), $C^c_{2,\Psi_{i1}} = Kh^{\mu+1}(r^2_{2,\Psi_{i1}}+h^2)^{-\frac{\mu+3}{2}}\Gamma(r_{2,\Psi_{i1}})$, $C^c_{2,\Psi_{i2}} = Kh^{\mu+1}(r^2_{2,\Psi_{i2}}+h^2)^{-\frac{\mu+3}{2}}\Gamma(r_{2,\Psi_{i2}})$, $C^c_{2,\Psi_{m1}} = Kh^{\mu+1}(r^2_{2,\Psi_{m1}}+h^2)^{-\frac{\mu+3}{2}}\Gamma(r_{2,\Psi_{m1}})$, $C^c_{2,\Psi_{m2}} = Kh^{\mu+1}(r^2_{2,\Psi_{m2}}+h^2)^{-\frac{\mu+3}{2}}\Gamma(r_{2,\Psi_{m2}})$, $\Psi_{m1} = \frac{(m-1)\pi}{2}+\tan^{-1}(\frac{T}{T-1})$ and $\Psi_{m2} = \frac{m\pi}{2}-\tan^{-1}(\frac{T}{T-1})$, $r_{2,\Psi_{i1}} = \sqrt{r_0^2+4d^2-4r_0d\cos(\Psi_{i1}-\alpha)}$, $r_{2,\Psi_{i2}} = \sqrt{r_0^2+8d^2-4\sqrt{2}r_0d\cos(\Psi_{i2}-\alpha)}$, $r_{2,\Psi_{m1}} = \sqrt{r_0^2+5d^2-2\sqrt{5}r_0d\cos(\Psi_{m1}-\alpha)}$, and $r_{2,\Psi_{m2}} = \sqrt{r_0^2+5d^2-2\sqrt{5}r_0d\cos(\Psi_{m2}-\alpha)}$. The result above can be generalized:

$$\begin{aligned} I^c_c(r,h,\alpha) &= I^c_{c(T-1)} + I^c_{c(T)} \\ &= I^c_{c(T-1)} + \sum_{i=1}^{4}\left(C^c_{T,\Psi_{i1}}+C^c_{T,\Psi_{i2}}\right) \\ &\quad + \sum_{t=1}^{T-1}\sum_{m=1}^{4}\left(C^c_{T,\Psi_{tm1}}+C^c_{T,\Psi_{tm2}}\right) \end{aligned} \tag{37}$$

where $C^c_{T,\Psi_{i1}} = Kh^{\mu+1}(r^2_{T,\Psi_{i1}}+h^2)^{-\frac{\mu+3}{2}}\Gamma(r_{T,\Psi_{i1}})$, $C^c_{T,\Psi_{i2}} = Kh^{\mu+1}(r^2_{T,\Psi_{i2}}+h^2)^{-\frac{\mu+3}{2}}\Gamma(r_{T,\Psi_{i2}})$, $C^c_{T,\Psi_{tm1}} = Kh^{\mu+1}(r^2_{T,\Psi_{tm1}}+h^2)^{-\frac{\mu+3}{2}}\Gamma(r_{T,\Psi_{tm1}})$, and $C^c_{T,\Psi_{tm2}} = Kh^{\mu+1}(r^2_{T,\Psi_{tm2}}+h^2)^{-\frac{\mu+3}{2}}\Gamma(r_{T,\Psi_{tm2}})$. $r_{T,\Psi_{tm1}} = \sqrt{r_0^2+D^2_{T,\Psi_{tm}}-2r_0D_{T,\Psi_{tm}}\cos(\Psi_{tm1}-\alpha)}$, $r_{T,\Psi_{tm2}} = \sqrt{r_0^2+D^2_{T,\Psi_{tm}}-2r_0D_{T,\Psi_{tm}}\cos(\Psi_{tm2}-\alpha)}$,

$\Psi_{tm1} = \frac{(m-1)\pi}{2} + \tan^{-1}\left(\frac{t}{T}\right)$, $\Psi_{tm2} = \frac{m\pi}{2} - \tan^{-1}\left(\frac{t}{T}\right)$, and $D_{T,\Psi_{tm}} = \sqrt{(T^2+t^2)}d$.

Note that when evaluating the interference from all nodes for $T = 3$, Eq. (37) is applied sequentially for $T = 1$, $T = 2$, and $T = 3$. The total interference for an arbitrary number of tiers can be obtained in a similar manner. UE located at height h may experience interference from all or a subset of nodes in the first tier if the closest interferer lies within the receiver field-of-view, i.e., $\min(r_{1,0}) \leq h\tan(\theta_r)$. Since neighbouring nodes are separated by a distance d, the minimum distance between UE and the closest interferer in the first tier is $\frac{d}{2}$. Similarly, interference from the second tier occurs when $\min(r_{2,0}) \leq h\tan(\theta_r)$, where $\min(r_{2,0}) = \frac{3d}{2}$. Consequently, the maximum number of tiers contributing to interference occurs when UE is located at the maximum height, i.e., $h = h_n$.

$$T = 2\left\lfloor \frac{\frac{2h_n\tan(\theta_r)}{d} - 1}{2} \right\rfloor + 1 \tag{38}$$

where $\lfloor\cdot\rfloor$ denotes the floor function. Since the UE location is random within the system, the interference caused by any node depends on the distance-dependent random variables associated with its position, namely (r_0, h, α). From Definition 3, the expected interference in the cell-centre region can therefore be expressed as:

$$\mathbb{E}[I_c^c] = \int_{\mathbb{D}_c^c} I_c^c(r,h,\alpha)\; f_c^c(r,h,\alpha)\, d\mathbb{D}_c^c \tag{39}$$

where $\mathbb{D}_c^c$ denotes the bounded spatial domain of the cell-centre region in the core zone, and $f_c^c(r,h,\alpha)$ represents the joint density of the random variables r_0, h, and α, whose support corresponds to the cell-centre region. Since the cell-centre region is considered, UE is located at a distance of at most $\frac{d}{2}$ from the serving node, as illustrated in Fig. 4. Conditioned on UE being located in the core zone and within the cell-centre region, the CDF of the distance r_0 from the serving node, for $0 \leq r_0 \leq \frac{d}{2}$, is obtained from the corresponding area ratio, as defined in Definition 1, and is given by

$$F_c^c(r) = \frac{A_{034}}{A_{012}} \tag{40}$$

where $A_{034} = \frac{\pi r^2}{8}$ denotes the area of sector 034 centred at the serving node, and $A_{012} = \frac{d^2}{8}$ denotes the area of triangle 012, i.e., the spatial domain of the cell-centre region under consideration. The corresponding density of r_0 is then obtained by differentiating $F_c^c(r)$ with respect to r:

$$\begin{aligned} f_c^c(r) &= \frac{d}{dr}F_c^c(r) \\ &= \frac{2\pi r}{d^2} \end{aligned} \tag{41}$$

The distribution of the interference also depends on the random variable α. From geometric considerations, α takes values in the range $[0, \frac{\pi}{4}]$. Since UE is uniformly distributed within the cell-centre region, and the variables r_0 and h do not influence the distribution of α in this region, α can be treated as an independent random variable with a uniform distribution over $[0, \frac{\pi}{4}]$. Therefore, the conditional PDF of α is given by:

$$f_c^c(\alpha) = \frac{4}{\pi} \tag{42}$$

Since UE can be at any height between h_c and h_n, h can be assumed independent and uniformly distributed over interval $[h_c, h_n]$. Therefore, PDF of h is given by:

$$f_c^c(h) = \frac{1}{h_n - (h_n - h_c)} \tag{43}$$

Note that some dependence may exist between certain random variables (e.g., r_0 and α) in the cell-edge region, as discussed in the next theorem. However, in the cell-centre region, these variables are governed by independent geometric constraints, and no such dependence arises. Consequently, r_0, h, and α can be treated as independent random variables in this region, and the joint density can therefore be obtained according to Definition 2:

$$\begin{aligned} f_c^c(r,h,\alpha) &= f_c^c(r) f_c^c(h) f_c^c(\alpha) \\ &= \frac{8r}{d^2 h_c} \end{aligned} \tag{44}$$

By substituting Eq. (44) and Eq. (37) into Eq. (39), expected value of interference is obtained in Eq. (13). ■

Appendix B

Consider UE located at a distance r_0 from the centre of the serving node, where $\frac{d}{2} < r_0 \leq \frac{d}{\sqrt{2}}$, as illustrated in Fig. 5. In this region, some nodes that contribute to interference at the cell centre may have a reduced or negligible impact at the cell edge due to the UE's proximity to other nearby nodes. However, the number of tiers and the set of potential interfering nodes are determined in Theorem 1 based on a worst-case scenario, corresponding to UE being located at the cell edge. Furthermore, any node within these tiers that does not contribute to interference at a given UE location is effectively excluded by the FOV constraint in (11) during the interference evaluation. Therefore, it is appropriate to determine the number of tiers and potential interfering nodes in the same manner as in Theorem 1. The analytical expression of the interference for a UE located at a distance r_0 from the serving node is given by:

$$\begin{aligned} I_e^c(r,\alpha,h) &= I_{e(T-1)}^c + I_{e(T)}^c \\ &= I_{e(T-1)}^c + \sum_{i=1}^{4}\left(E_{T,\Psi_{i1}} + E_{T,\Psi_{i2}}\right) + \\ &\qquad \sum_{t=1}^{T-1}\sum_{m=1}^{4}\left(E_{T,\Psi_{tm1}} + E_{T,\Psi_{tm2}}\right) \\ &= I_c^c(r,\alpha,h) \end{aligned} \tag{45}$$

where $I_{e(T-1)}^c$ and $I_{e(T)}^c$ denote the interference contributions from the first $(T-1)$ tiers and the Tth tier, respectively. The term $E_{T,\star}$ represents the interference contribution at

the cell edge from node $N_{T,\Psi_\star}$ in the Tth tier, located at an angular position $0 \leq \star < 2\pi$. The term $I_c^c(r,\alpha,h)$ denotes the analytical expression of the interference obtained in Theorem 1, and T is the total number of tiers contributing to interference, as defined in Theorem 1.

Since UE location is random, these parameters are modelled as random variables. The expected interference at the cell edge is therefore obtained by averaging over their joint distribution. Conditioned on UE being located in the core zone and within the cell-edge region, the CDF of the distance r_0 from the serving node, for $\frac{d}{2} < r_0 \leq \frac{d}{\sqrt{2}}$, is obtained from the corresponding area ratio based on Definition 1. The corresponding density is then expressed as:

$$\begin{aligned} f_e^c(r) &= \frac{d}{dr}F_e^c(r) \\ &= \frac{d}{dr}\frac{A_{1654}(r)}{A_{021}} \\ &= \frac{d}{dr}\frac{A_{1653}(r)-A_{143}(r)}{A_{021}} \\ &= \frac{1}{A_{021}}\frac{d}{dr}\big(\underbrace{(A_{035}(r)-A_{061})}_{A_{1653}(r)} - \underbrace{(A_{043}(r)-A_{041}(r))}_{A_{143}(r)}\big) \\ &= \frac{1}{A_{021}}\frac{d}{dr}\Bigg(\big(\underbrace{\frac{r^2\pi}{8}}_{A_{053}(r)}\big) - \big(\underbrace{\frac{d^2\pi}{32}}_{A_{061}}\big) - \big(\underbrace{\frac{r^2\cos^{-1}(d/2r)}{2}}_{A_{043}(r)}\big) \\ &\qquad - \big(\underbrace{\frac{d\sqrt{r^2-d^2/4}}{4}}_{A_{041}(r)}\big)\Bigg) \\ &= \frac{2r}{d^2}\big(\pi - 4\cos^{-1}\big(\frac{d}{2r}\big)\big) \end{aligned} \tag{46}$$

where $\frac{A_{1654}(r)}{A_{021}}$ denotes the probability that UE is located at a distance less than or equal to r from the serving node, conditioned on UE being in the cell-edge region of the core zone. Here, A_{021} represents the spatial domain of the cell-edge region under consideration. $A_{1654}(r) = A_{1653}(r) - A_{143}(r)$ is the area where UE can be in the edge area, $A_{021} = d^2/8$ is the total area of interest, $A_{1653}(r)$ is the area of annulus sector 1653 and obtained by subtracting the area of sector 061 (A_{061}) from the area of sector 053 ($A_{053}(r)$), $A_{143}(r)$ is the area located in annulus sector 1653 but part of the neighbouring cell (closest interferer cell) and can be obtained by subtracting the area of triangle 041 (A_{041}) from the area of sector 043 ($A_{043}(r)$).

The angle α has a different distribution in the edge region due to the cell boundaries. From observation, α depends on the value of r_0, for instance, when $r_0 > \frac{d}{2}$ (which is the case in the cell edge area as $\frac{d}{2} < r_0 \leq \frac{d}{\sqrt{2}}$), α can not take the value of 0. Furthermore, α can not take a value less than $\frac{\pi}{4}$ when $r_0 = \frac{d}{\sqrt{2}}$. Actually, α is uniformly distributed in the range α_{min} to α_{max} where $\alpha_{min} = \cos^{-1}\left(\frac{d}{2r}\right)$ is the minimum value that α can take at r_0 and $\alpha_{max} = \frac{\pi}{4}$. Therefore, the conditional PDF of α can be expressed by:

$$f_e^c(\alpha|r_0) = \frac{1}{\alpha_{max}-\alpha_{min}} \tag{47}$$

From Definition 4, the joint PDF of r_0 and α can be obtained by:

$$\begin{aligned} f_e^c(r,\alpha) &= f_e^c(\alpha|r_0)f_e^c(r) \\ &= \frac{\big(2r\pi - 8r\cos^{-1}\left(\frac{d}{2r}\right)\big)}{\big(\alpha_{max}-\alpha_{min}\big)d^2} \end{aligned} \tag{48}$$

since UE can be at any height from h_n to $h_n - h_c$ regardless the values of r_0 and α in the cell edge area, h is uniformly distributed in the range of h_n to $h_n - h_c$. Therefore, the joint density of three random variables r_0, α and h can be expressed by:

$$f_e^c(r,\alpha,h) = f_e^c(r,\alpha)\cdot f_e^c(h) \tag{49}$$

where $f_e^c(h) = \frac{1}{h_c}$. The expected value of interference can be expressed by:

$$\mathbb{E}[I_e^c] = \int_{\mathbb{D}_e^c} I_e^c(r,h,\alpha)\ f_e^c(r,h,\alpha)\, d\mathbb{D}_e^c \tag{50}$$

where where $\mathbb{D}_e^c$ is the bounded spatial domain of the cell edge in the core zone. The expected value of interference is reached in Eq. (17). ■

Appendix C

The characteristics of the interference in the mid zone are similar to those in the core zone. However, the key difference lies in the reduced number of potential interfering nodes due to the presence of the system boundary. For instance, when UE is located in the last row of the mid zone (specifically in the half further from the system boundary), nodes from different tiers located within the angular range $\left[\frac{\pi}{2}+\tan^{-1}\left(\frac{1}{T}\right),,\frac{3\pi}{2}-\tan^{-1}\left(\frac{1}{T}\right)\right]$ do not contribute to interference, where T denotes the number of interfering tiers. The mid zone extends up to T tiers from the system boundary, excluding the half of the last cell adjacent to the boundary, which belongs to the boundary zone. Each cell within the mid zone is therefore divided into two halves—closer and further from the boundary—except for the last cell, which includes only the further half. As a result, the total number of cell halves in the mid zone is $2T-1$, and the probability of UE being located in any given half is $\frac{1}{2T-1}$. Conditioned on UE being located in the further half of the last cell and at a distance r_0 from its serving node, the analytical expression of the interference can be written as:

$$I_c^{m(1)}(r,\alpha,h) = \frac{I^c_{c/N_{:,\Phi}:\Phi\in\left[\frac{\pi}{2}+\tan^{-1}\left(\frac{1}{T}\right),\ \frac{3\pi}{2}-\tan^{-1}\left(\frac{1}{T}\right)\right]}}{2T-1} \tag{51}$$

where $I^c_{c/N_{:,\Phi}}$ denotes the interference in the core area (derived in Eq. (14)) excluding the nodes located in the angular range $\left[\frac{\pi}{2}+\tan^{-1}\left(\frac{1}{T}\right),\frac{3\pi}{2}-\tan^{-1}\left(\frac{1}{T}\right)\right]$. The interference at other rows of the mid-area varies depending on the UE's position within the cell. For example, if UE is located in the

second-to-last row, the interference will differ depending on whether it lies in the far half (towards the network interior) or the near half (towards the system boundary). If UE is in the far half, the interferers located in the angular range $\left[\frac{\pi}{2}+\tan^{-1}\left(\frac{2}{T}\right), \frac{3\pi}{2}-\tan^{-1}\left(\frac{2}{T}\right)\right]$ are excluded. If UE is in the near half, the interferers located in the angular range $\left[-\tan^{-1}\left(\frac{2}{T}\right), \tan^{-1}\left(\frac{2}{T}\right)\right]$ are excluded. Accordingly, the interference experienced by UE in the second-to-last row is given by

$$I_c^{m(2)}(r,\alpha,h)=\frac{1}{2T-1}\left(I^c_{c/N_{:,\Phi 1}}+I^c_{c/N_{:,\Phi 2}}\right). \tag{52}$$

$\Phi 1 \in \left[\frac{\pi}{2}+\tan^{-1}\left(\frac{2}{T}\right), \frac{3\pi}{2}-\tan^{-1}\left(\frac{2}{T}\right)\right]$ and $\Phi 2 \in \left[-\tan^{-1}\left(\frac{2}{T}\right), \tan^{-1}\left(\frac{2}{T}\right)\right]$. Since UE is assumed to be randomly located within the system, given that it lies in any where in the cell centre of the mid zone, the interference can be expressed as

$$I_c^{m}(r,\alpha,h)=\frac{1}{2T-1}\left(\sum_{i=1}^{T} I^c_{c/N_{:,\Phi 1}}+\sum_{m=2}^{T} I^c_{c/N_{:,\Phi 2}}\right). \tag{53}$$

where $\Phi 1 \in \left[\frac{\pi}{2}+\tan^{-1}\left(\frac{i}{T}\right), \frac{3\pi}{2}-\tan^{-1}\left(\frac{i}{T}\right)\right]$ and $\Phi 2 \in \left[-\tan^{-1}\left(\frac{m}{T}\right), \tan^{-1}\left(\frac{m}{T}\right)\right]$. Note that UE can also be in the cell edge. It is discussed in Theorem 2 that the potential interfering nodes from different tires are the same in the cell edge. Therefore, the total interference experienced by UE in the cell edge of the mid zone can be expressed by

$$I_e^{m}(r,\alpha,h)=\frac{1}{2T-1}\left(\sum_{i=1}^{T} I^c_{e/N_{:,\Phi 1}}+\sum_{m=2}^{T} I^c_{e/N_{:,\Phi 2}}\right). \tag{54}$$

The expected interference when UE located anywhere in the mid zone can be expressed by

$$\mathbb{E}[I^m]=\int_{\mathbb{D}_c^m} I_c^m(r,h,\alpha)\; f_c^m(r,h,\alpha)\, d\mathbb{D}_c^m+ \int_{\mathbb{D}_e^m} I_e^m(r,h,\alpha)\; f_e^m(r,h,\alpha)\, d\mathbb{D}_e^m \tag{55}$$

where $\mathbb{D}_c^m$ and $\mathbb{D}_e^m$ are the bounded spatial domain of the cell centre and edge in the mid zone respectively. Since the distance random variables have the same distribution as in the core zone, $f_c^m(r,h,\alpha)=f_c^c(r,h,\alpha)$ and $\mathbb{D}_c^m=\mathbb{D}_c^c$ which are obtained in Theorem 1 and $f_e^m(r,h,\alpha)=f_e^c(r,h,\alpha)$ and $\mathbb{D}_e^m=\mathbb{D}_e^c$ which are obtained in Theorem 2. The final results are reached ■

Appendix D

Assume that UE is located within the boundary zone, as illustrated in Fig. 6, where the distance between the outermost nodes and the system boundary is denoted by $\acute{d}$. In this zone, the distributions of the distance-dependent parameters, such as r_0 and α, are more complex compared with the core and mid zones. This complexity arises because $\acute{d}$ can take different values relative to the inter-node distance d, i.e., $\acute{d}<\frac{d}{2}$, $\acute{d}=\frac{d}{2}$, or $\acute{d}>\frac{d}{2}$. When $\acute{d}\neq\frac{d}{2}$, accurately modelling the interference requires a detailed geometric characterisation of the cell. Accordingly, the cell is partitioned into three distinct regions—centre, middle, and edge—as shown in Fig. 6, each associated with different distance constraints and interference characteristics. Therefore, the interference in each region must be analysed separately. The expected interference in the boundary zone can thus be expressed as:

$$\begin{aligned}\mathbb{E}[I^b]=&\int_{\mathbb{D}_c^b} I_c^b(r,h,\alpha)\; f_c^b(r,h,\alpha)\, d\mathbb{D}_c^b+\\ &\int_{\mathbb{D}_m^b} I_m^b(r,h,\alpha)\; f_m^b(r,h,\alpha)\, d\mathbb{D}_b^m+\\ &\int_{\mathbb{D}_e^b} I_e^b(r,h,\alpha)\; f_e^b(r,h,\alpha)\, d\mathbb{D}_e^b\end{aligned} \tag{56}$$

where $I_c^b(r,h,\alpha)$, $I_m^b(r,h,\alpha)$, and $I_e^b(r,h,\alpha)$ denote the analytical expressions of the interference in the centre, middle, and edge regions of the boundary zone, respectively. The domains $\mathbb{D}_c^b$, $\mathbb{D}_m^b$, and $\mathbb{D}_e^b$ represent the corresponding bounded spatial regions, while $f_c^b(r,h,\alpha)$, $f_m^b(r,h,\alpha)$, and $f_e^b(r,h,\alpha)$ denote the joint densities of the distance-dependent parameters in these regions. Similar to the mid zone, some interfering nodes are excluded when evaluating the interference in the boundary zone due to the absence of nodes beyond the system boundary. When UE is located in this zone, the analytical expression of the interference can be obtained as follows:

$$I_c^b(r,h,\alpha)=I^c_{c/N_{:,\Phi:\frac{\pi}{2}<\Phi<\frac{3\pi}{2}}} \tag{57}$$

where $I^c_{c/N_{:,\Phi:\frac{\pi}{2}<\Phi<\frac{3\pi}{2}}}$ denotes the analytical expression of the interference in the core region (derived in Eq. (14)) after excluding nodes located within the angular range $\frac{\pi}{2}<\Phi<\frac{3\pi}{2}$. As discussed in Theorem 2, the set of potential interfering nodes from different tiers remains the same across the different regions of the cell. This is because nodes that do not contribute to interference at a given UE location are effectively filtered out by the FOV constraint in Eq. (11), depending on the values of r_0 and the corresponding distances to the interfering nodes. Therefore, the analytical expression of the aggregate interference for the other cell regions can be expressed as:

$$I_c^b(r,h,\alpha)=I_m^b(r,h,\alpha)=I_e^b(r,h,\alpha) \tag{58}$$

It is important to note that Eq. (58) refers to the analytical form of the interference expression and the set of potential interfering nodes, which are identical across these regions. However, the actual interference experienced by UE varies spatially due to differences in the distance-dependent parameters r_0, h, and α, as well as the spatial weighting introduced by the corresponding joint PDFs.

Assume that $\acute{d}<\frac{d}{2}$. In this case, the random variables r_0 and α follow different distributions in the centre, middle, and edge regions of the cell, as illustrated in Fig. 6. Conditioned on UE being located in the boundary zone and within the cell-centre region, the density of r_0 is derived from the

corresponding area ratio, as defined in Definition 1, and can be obtained similarly to Theorem 1:

$$\begin{aligned} f_c^b(r) &= \frac{d}{dr}F_c^b(r) \\ &= \frac{d}{dr}\Big(\frac{A_{045}(r)}{A_{0123}}\Big) \\ &= \frac{\pi r}{d\acute{d}} \end{aligned} \tag{59}$$

where $A_{0123} = \frac{d\acute{d}}{2}$ denotes the spatial domain of the cell-centre region under consideration, and $A_{045}(r) = \frac{\pi/2}{2\pi}\pi r^2$ denotes the area of sector 045, for $0 \leq r \leq \acute{d}$. In the centre region, α is randomly distributed in the range of 0 to $\frac{\pi}{2}$ and PDF of α is $\frac{2}{\pi}$. The height of UE is assumed to be independent and uniformly distributed over the interval $[h_c, h_n]$. From Definition 2, the joint density of r_0 and α in the centre region can be obtained by:

$$\begin{aligned} f_c^b(r,\alpha,h) &= f_c^b(r)f_c^b(\alpha)f_c^b(h) \\ &= \frac{2r}{dh_c\acute{d}} \end{aligned} \tag{60}$$

The middle region arises when r_0 takes values in the range $\acute{d} < r_0 \leq \frac{d}{2}$, as illustrated in Fig. 6(b). Conditioned on UE being located in the boundary zone and within the cell-middle region, the density of r_0 can be obtained from the corresponding area ratio, as defined in Definition 1:

$$\begin{aligned} f_m^b(r) &= \frac{d}{dr}F_m^b(r) \\ &= \frac{d}{dr}\Big(\frac{A_{1674}(r)}{A_{0123}}\Big) \\ &= \frac{d}{dr}\Big(\frac{A_{057}(r) - A_{014} - A_{156}(r)}{A_{0123}}\Big) \\ &= \frac{1}{A_{0123}}\frac{d}{dr}\Big(A_{057}(r) - A_{014} - (\underbrace{A_{056}(r) - A_{016}(r)}_{A_{156}(r)})\Big) \\ &= \frac{1}{A_{0123}}\frac{d}{dr}\Big(\underbrace{(\frac{\pi/2}{2\pi}\pi r^2)}_{A_{057}(r)} - \underbrace{(\frac{\pi/2}{2\pi}\pi\acute{d}^2)}_{A_{014}} - \\ &\qquad \underbrace{(\frac{\cos^{-1}(\acute{d}/2r)}{2\pi}\pi r^2)}_{A_{056}(r)} - \underbrace{(\frac{\acute{d}\sqrt{r^2-\acute{d}^2}}{2})}_{A_{016}(r)}\Big) \\ &= \frac{r}{d\acute{d}}\big(\pi - 2\cos^{-1}\big(\frac{\acute{d}}{r}\big)\big) \end{aligned} \tag{61}$$

where $F_m^b(r) = \frac{A_{1674}(r)}{A_{0123}}$ denotes the cumulative probability that UE is located at a distance less than or equal to r from the serving node, within the cell-middle region of the boundary zone. $A_{1674}(r) = A_{057}(r) - A_{014} - A_{156}(r)$ is the area where UE can be in the middle zone, $A_{0123} = \frac{d\acute{d}}{2}$ is the total area of interest, $A_{057}(r)$ is the area of sector 057, A_{014} is total area of centre region, $A_{156}(r)$ is area part of the sector 057 but located out of interest area 0123. $A_{156}(r)$ can be obtained by subtracting the area of triangle of 016 from the area of sector 056.

Unlike the angle α in the centre region, α has a different distribution in the middle region of the cell. α depends on the value of r_0. α is uniformly distributed in the range α_{min} to α_{max} where $\alpha_{min} = 0$ is the minimum value that α can take at r_0 and $\alpha_{max} = \frac{\pi}{2} - \cos^{-1}\big(\frac{\acute{d}}{r}\big)$. Therefore, the conditional PDF of α can be expressed by:

$$f_m^b(\alpha|r) = \frac{1}{\alpha_{max} - \alpha_{min}} \tag{62}$$

From Definition 4 and Definition 2, the joint PDF of $f_m^b(r,\alpha,h)$ can be obtained by:

$$f_m^b(r,\alpha,h) = f_m^b(r)f_m^b(\alpha|r)f_m^b(h) \tag{63}$$

The edge region corresponds to the case where r_0 takes values in the range $\frac{d}{2} < r_0 \leq \sqrt{\acute{d}^2 + \frac{d^2}{4}}$, as illustrated in Fig. 6(c). Conditioned on UE being located in the boundary zone and within the cell-edge region, the density of r_0 can be obtained from the corresponding area ratio, as defined in Definition 1:

$$\begin{aligned} f_e^b(r) &= \frac{d}{dr}F_e^b(r) \\ &= \frac{d}{dr}\Big(\frac{A_{6783}(r)}{A_{0123}}\Big) \\ &= \frac{d}{dr}\Big(\frac{A_{059}(r) - A_{0163} - A_{157}(r) - A_{893}(r)}{A_{0123}}\Big) \\ &= \frac{1}{A_{0123}}\frac{d}{dr}\Big(A_{059}(r) - A_{0163} - (\underbrace{A_{057}(r) - A_{017}(r)}_{A_{157}(r)}) \\ &\qquad - (\underbrace{A_{089}(r) - A_{083}(r)}_{A_{893}(r)})\Big) \\ &= \frac{1}{A_{0123}}\frac{d}{dr}\Big(\underbrace{(\frac{\pi}{4}r^2)}_{A_{059}(r)} - A_{0163} - (\underbrace{\frac{\cos^{-1}(\acute{d}/r)}{2\pi}\pi r^2}_{A_{057}}) \\ &\qquad - \underbrace{(\frac{\acute{d}\sqrt{r^2-\acute{d}^2}}{2})}_{A_{017}(r)} - \underbrace{(\frac{\cos^{-1}(d/2r)}{2\pi}\pi r^2)}_{A_{089}(r)} - \\ &\qquad \underbrace{(\frac{d\sqrt{r^2-d^2/4}}{4})}_{A_{038}(r)}\Big) \\ &= \frac{2r}{d\acute{d}}\Big(\frac{\pi}{2} - \cos^{-1}\big(\frac{\acute{d}}{r}\big) - \cos^{-1}\big(\frac{d}{2r}\big)\Big) \end{aligned} \tag{64}$$

where $F_e^b(r) = \frac{A_{6783}(r)}{A_{0123}}$ denotes the cumulative probability that UE is located at a distance less than or equal to r from the serving node, within the cell-edge region of the boundary zone. $A_{6783}(r) = A_{059}(r) - A_{0163} - A_{157}(r) - A_{893}(r)$ is the area where UE can be in the edge area, $A_{0123} = \frac{d\acute{d}}{2}$ is the total area of interest, $A_{059}(r)$ is the area of sector 059, A_{0163} is total area of centre and intermediate regions, $A_{157}(r)$ and $A_{893}(r)$ the areas part of the sector 059 but located out of interest area 0123. $A_{157}(r)$ is obtained by subtracting the area of triangle of 017 from the area of sector 057 and

$A_{893}(r)$ is obtained by subtracting the area of triangle of 083 from the area of sector 089.

α depends on the value of r_0 and is uniformly distributed in the range α_{min} to α_{max} where $\alpha_{min} = \arccos(d/2r)$ is the minimum value that α can take at r_0 and $\alpha_{max} = \frac{\pi}{2} - \cos^{-1}\left(\frac{d}{r}\right)$. Therefore, the conditional PDF of α can be expressed by:

$$f_e^b(\alpha|r) = \frac{1}{\alpha_{max} - \alpha_{min}} \tag{65}$$

From Definition 4 and Definition 2, the joint density of $f_e^b(r, \alpha, h)$ can be obtained by:

$$f_e^b(r, \alpha, h) = f_e^b(r) f_e^b(\alpha|r) f_e^b(h) \tag{66}$$

The results in Eq. (21) is reached when substituting Eq. (57), Eq. (60), Eq. (63) and Eq. (66) in Eq. (56). ■

Appendix E

When a reuse factor of 3 is applied, the minimum distance to the closest co-channel interferer increases from $\frac{d}{2}$ to $\frac{3d}{2}$. Consequently, cells in the first tier do not reuse the same resources, and the cell of interest does not experience interference from tiers $1, 3, 5, \ldots$. Furthermore, only a subset of nodes in the remaining tiers (e.g., tiers $2, 4, \ldots$) contribute to interference. As a result, the effective number of interfering tiers is reduced to $\frac{\acute{T}}{2}$, where $\acute{T} = 2\left\lfloor \frac{T}{2} \right\rfloor$ and $\lfloor \cdot \rfloor$ denotes the floor function. Therefore, the analytical expression of the aggregate interference in the cell-centre region of the core zone can be obtained in a similar manner to Theorem 1:

$$I_c^{c3}(r, h, \alpha) = I_{c(\acute{T}-2)}^{c3} + Kh^{\mu+1} \sum_{i=1}^{4} \left(C_{\acute{T},\Psi_{i1}}^c + C_{\acute{T},\Psi_{i2}}^c\right) + \sum_{t=2,4,\cdots}^{\acute{T}-2} \sum_{m=1}^{4} \left(C_{\acute{T},\Psi_{tm1}}^c + C_{\acute{T},\Psi_{tm2}}^c\right) \tag{67}$$

where $I_{c(\acute{T}-2)}^{c3}$ is the aggregate interference when the total number of interfering tiers is $\acute{T} - 2$, $C_{\acute{T},\Psi_\star}^c$ represents the interference experienced in the cell centre from the $N_{\acute{T},\Psi_\star}$ located at distance $r_{\acute{T},\Psi_\star}$ and angle $\Psi_\star$, $C_{\acute{T},\Psi_{i1}}^c = \left(r_{\acute{T},\Psi_{i1}}^2 + h^2\right)^{-\frac{\mu+3}{2}} \Gamma(r_{\acute{T},\Psi_{i1}})$, $C_{\acute{T},\Psi_{i2}}^c = \left(r_{\acute{T},\Psi_{i2}}^2 + h^2\right)^{-\frac{\mu+3}{2}} \Gamma(r_{\acute{T},\Psi_{i2}})$, $C_{\acute{T},\Psi_{tm1}}^c = \left(r_{\acute{T},\Psi_{tm1}}^2 + h^2\right)^{-\frac{\mu+3}{2}} \Gamma(r_{\acute{T},\Psi_{tm1}})$ and $C_{\acute{T},\Psi_{tm2}}^c = \left(r_{\acute{T},\Psi_{tm2}}^2 + h^2\right)^{-\frac{\mu+3}{2}} \Gamma(r_{\acute{T},\Psi_{tm2}})$. The corresponding values of $r_{\acute{T},\Psi_\star}$ and $\Psi_\star$ are obtained as in Theorem 1.

The set of potential interfering nodes in the cell-edge region is identical to that in the cell-centre region of the core zone. Accordingly, the analytical expressions satisfy $I_c^{c3}(r, h, \alpha) = I_e^{c3}(r, h, \alpha)$. It is noted that this equality refers to the analytical structure of the interference expression, while the actual interference values may differ due to variations in the distance-dependent parameters and their distributions. Similarly, the analytical expression of the interference for UE located in the cell-centre region of the mid zone can be obtained as:

$$I_c^{m3}(r, h, \alpha) = \frac{1}{2T-1}\left(\sum_{i=1}^{T} I_{c/N_{:,\Phi 1}}^{c3} + \sum_{m=2}^{T} I_{c/N_{:,\Phi 2}}^{c3}\right). \tag{68}$$

where $\Phi 1 \in \left[\frac{\pi}{2} + \tan^{-1}\left(\frac{i}{T}\right), \frac{3\pi}{2} - \tan^{-1}\left(\frac{i}{T}\right)\right]$ and $\Phi 2 \in \left[-\tan^{-1}\left(\frac{m}{T}\right), \tan^{-1}\left(\frac{m}{T}\right)\right]$. It is noted that UE may also be located in the cell-edge region. As discussed in Theorem 2, the set of potential interfering nodes from different tiers remains the same in the cell-edge region. Accordingly, the analytical expressions satisfy $I_c^{m3}(r, h, \alpha) = I_e^{m3}(r, h, \alpha)$. This equality reflects the identical analytical structure of the interference expression, while the actual interference values may differ due to variations in the distance-dependent parameters and their distributions. The interference in the cell centre of the boundary zone can be obtained similar to Theorem 4:

$$I_c^{b3}(r, h, \alpha) = I_{c/N_{:,\Phi}:\frac{\pi}{2}>\Phi>\frac{3\pi}{2}}^{c3} \tag{69}$$

where $I_{c/N_{:,\Phi}:\frac{\pi}{2}>\Phi>\frac{3\pi}{2}}^{c3}$ denotes the interference in the core area obtained in Eq.(67) excluding the nodes located in the angle between $\frac{\pi}{2}$ and $\frac{3\pi}{2}$. The potential number of interfering nodes is the same across the different areas of the boundary zone, therefore $I_c^{b3}(r, h, \alpha) = I_e^{b3}(r, h, \alpha)$ when $\acute{d} = \frac{d}{2}$ and $I_c^{b3}(r, h, \alpha) = I_m^{b3}(r, h, \alpha) = I_e^{b3}(r, h, \alpha)$ when $\acute{d} \neq \frac{d}{2}$

Note that the expected value of the interference in each region can be obtained using the same joint densities derived in the previous subsections. Unlike the set of potential interfering nodes, the distributions of the distance-dependent parameters are not affected by the reuse factor. Accordingly, the expected interference in the zth zone, where $a \in c, m, b$, can be expressed as:

$$\begin{aligned}\mathbb{E}[I^{z3}] = &\int_{\mathbb{D}_c^{z3}} I_c^{z3}(r, h, \alpha)\ f_c^{z3}(r, h, \alpha)\, d\mathbb{D}_c^{z3} + \\ &\Gamma(\acute{d}) \int_{\mathbb{D}_m^{z3}} I_m^{z3}(r, h, \alpha)\ f_m^{z3}(r, h, \alpha)\, d\mathbb{D}_{z3}^{m} + \\ &\int_{\mathbb{D}_e^{z3}} I_e^{z3}(r, h, \alpha)\ f_e^{z3}(r, h, \alpha)\, d\mathbb{D}_e^{z3}\end{aligned} \tag{70}$$

where $\mathbb{D}_c^{z3} = \mathbb{D}_c^z$, $\mathbb{D}_m^{z3} = \mathbb{D}_m^z$ and $\mathbb{D}_e^{z3} = \mathbb{D}_e^z$ are the bounded spatial domain of the cell centre, middle and edge in zth zone respectively, and they are obtained in Theorem 1, 2, 3 and 4. $\Gamma(\acute{d})$ is expressed by:

$$\Gamma(\acute{d}) = \begin{cases} 1 & z = b\ \&\ \acute{d} \neq \frac{d}{2} \\ 0 & \text{otherwise} \end{cases} \tag{71}$$

$f_c^{z3}(r, h, \alpha) = f_c^z(r, h, \alpha)$, $f_m^{z3}(r, h, \alpha) = f_m^z(r, h, \alpha)$ and $f_e^{z3}(r, h, \alpha) = f_e^z(r, h, \alpha)$ are the joint densities in different areas of the cell of zth zone and obtained in Theorem 1, 2, 3 and 4. The final results in Eq. (26). ■

REFERENCES

[1] M. Z. Chowdhury, M. T. Hossan, A. Islam, and Y. M. Jang, "A comparative survey of optical wireless technologies: Architectures and applications," *IEEE Access*, vol. 6, pp. 9819–9840, 2018.

[2] A. Mahbas, J. Cosmas, and H. Al-Raweshidy, "Distance analysis in regular OWC deployments," *IEEE Access*, vol. 12, pp. 186803–186818, 2024.
[3] S. Bastiaens, M. Alijani, W. Joseph, and D. Plets, "A review of the quality of positioning service of VLP within the indoor positioning system landscape," *IEEE Trans. Instrum. Meas.*, vol. 75, pp. 1–33, 2026.
[4] A. Mahbas, J. Cosmas, S. Mueen, and J. Wang, "LOS analysis for localization in high frequency systems," *IEEE Trans. Wireless Commun.*, vol. 23, no. 6, pp. 6425–6437, Jun. 2024.
[5] A. J. Mahbas, H. Zhu, and J. Wang, "Impact of small cells overlapping on mobility management," *IEEE Trans. Wireless Commun.*, vol. 18, no. 2, pp. 1054–1068, Feb. 2019.
[6] C. Chen, D. A. Basnayaka, and H. Haas, "Downlink performance of optical attocell networks," *IEEE J. Lightw. Technol.*, vol. 34, no. 1, pp. 137–156, Jan. 2016.
[7] M. R. Ghaderi, "LiFi and hybrid WiFi/LiFi indoor networking: From theory to practice," *Opt. Switching Netw.*, vol. 47, 2023.
[8] S. Tao, H. Yu, Q. Li, and Y. Tang, "Derivation and analysis of probability distribution of visible-light channel gain difference based on Lambertian radiation," *IEEE Commun. Lett.*, vol. 24, no. 2, pp. 371–375, Feb. 2020.
[9] L. Yin, W. O. Popoola, X. Wu, and H. Haas, "Performance evaluation of non-orthogonal multiple access in visible light communication," *IEEE Trans. Commun.*, vol. 64, no. 12, pp. 5162–5175, Dec. 2016.
[10] Y. Zhou, N. Huang, and Z. Xu, "Outage and rate analysis for industrial Internet of Things in multitier visible light communication networks inside finite 3-D space," *IEEE Internet Things J.*, vol. 11, no. 11, pp. 20590–20604, Jun. 2024.
[11] H. Tabassum and E. Hossain, "Coverage and rate analysis for co-existing RF/VLC downlink cellular networks," *IEEE Trans. Wireless Commun.*, vol. 17, no. 4, pp. 2588–2601, Apr. 2018.
[12] L. Yin and H. Haas, "A tractable approach to joint transmission in multiuser visible light communication networks," *IEEE Trans. Mobile Comput.*, vol. 18, no. 10, pp. 2231–2242, Oct. 2019.
[13] L. Yin and H. Haas, "Coverage analysis of multiuser visible light communication networks," *IEEE Trans. Wireless Commun.*, vol. 17, no. 3, pp. 1630–1643, Mar. 2018.
[14] A. Vavoulas, H. G. Sandalidis, T. A. Tsiftsis, and N. Vaiopoulos, "Coverage aspects of indoor VLC networks," *IEEE J. Lightw. Technol.*, vol. 33, no. 23, pp. 4915–4921, Dec. 2015.
[15] X. Wu, M. D. Soltani, L. Zhou, M. Safari, and H. Haas, "Hybrid LiFi and WiFi networks: A survey," *IEEE Commun. Surveys Tuts.*, vol. 23, no. 2, pp. 1398–1420, 2nd Quart., 2021.
[16] M. Asad and S. Qaisar, "Energy efficient QoS-based access point selection in hybrid WiFi and LiFi IoT networks," *IEEE Trans. Green Commun. Netw.*, vol. 6, no. 2, pp. 897–906, Jun. 2022.
[17] A. Surampudi and R. K. Ganti, "Interference characterization in downlink Li-Fi optical attocell networks," *IEEE J. Lightw. Technol.*, vol. 36, no. 16, pp. 3211–3228, Aug. 2018.
[18] Shashikant, P. Garg, and P. K. Sharma, "Interference mitigation technique with coverage improvement in indoor VLC system," *Trans. Emerging Telecommun. Technol.*, vol. 30, no. 2, pp. 1–12, 2019.
[19] Y. Hei, X. Liu, W. Li, S. Wang, and M. Huo, "Energy- and spectral-efficiency tradeoff in nonlinear OFDM system of visible light communications," *IEEE J. Lightw. Technol.*, vol. 40, no. 7, pp. 1921–1929, Apr. 2022.
[20] B. Almeroth, A. J. Fehske, G. Fettweis, and E. Zimmermann, "Analytical interference models for the downlink of a cellular mobile network," in *Proc. IEEE GLOBECOM Workshops*, Houston, TX, USA, 2011, pp. 739–743.
[21] Z. Chen, D. A. Basnayaka, X. Wu, and H. Haas, "Interference mitigation for indoor optical attocell networks using an angle diversity receiver," *IEEE J. Lightw. Technol.*, vol. 36, no. 18, pp. 3866–3881, Sep. 2018.
[22] A. G. A. Al-Sakkaf and M. Morales-Céspedes, "Interference management for VLC indoor systems based on overlapping field-of-view angle diversity receivers," *IEEE Access*, vol. 12, pp. 51431–51449, 2024.
[23] A. G. Al-Sakkaf and M. Morales-Céspedes, "On the coverage footprint for high-capacity VLC through angle diversity receivers," in *Proc. IEEE GLOBECOM Workshops*, Kuala Lumpur, Malaysia, 2023, pp. 685–690.
[24] J. Li, X. Bao, W. Zhang, and N. Bao, "QoE probability coverage model of indoor visible light communication network," *IEEE Access*, vol. 8, pp. 45390–45399, 2020.
[25] N. Vaiopoulos, A. Vavoulas, and H. G. Sandalidis, "Impact of a randomly placed terminal on LiFi performance," *IEEE Trans. Commun.*, vol. 70, no. 3, pp. 1875–1885, Mar. 2022.
[26] G. Pan, J. Ye, and Z. Ding, "On secure VLC systems with spatially random terminals," *IEEE Commun. Lett.*, vol. 21, no. 3, pp. 492–495, Mar. 2017.
[27] J.-Y. Wang et al., "Performance analysis and improvement for secure VLC with SLIPT and random terminals," *IEEE Access*, vol. 8, pp. 73645–73658, 2020.
[28] G. Pan, H. Lei, Z. Ding, and Q. Ni, "3-D hybrid VLC-RF indoor IoT systems with light energy harvesting," *IEEE Trans. Green Commun. Netw.*, vol. 3, no. 3, pp. 853–865, Sep. 2019.
[29] S. Aboagye et al., "Multi-band wireless communication networks: Fundamentals, challenges, and resource allocation," *IEEE Trans. Commun.*, vol. 72, no. 7, pp. 4333–4383, Jul. 2024.
[30] T. Komine and M. Nakagawa, "Fundamental analysis for visible-light communication system using LED lights," *IEEE Trans. Consum. Electron.*, vol. 50, no. 1, pp. 100–107, Feb. 2004.
[31] J. Grubor, S. Randel, K.-D. Langer, and J. W. Walewski, "Broadband information broadcasting using LED-based interior lighting," *IEEE J. Lightw. Technol.*, vol. 26, no. 24, pp. 3883–3892, Dec. 2008.
[32] S. Dimitrov and H. Haas, "Throughput of cellular OWC networks," in *Principles of LED Light Communications: Towards Networked Li-Fi*. Cambridge, U.K.: Cambridge Univ. Press, 2015, pp. 151–182.
[33] A. Mahbas and J. Cosmas, "Experimental system design for optical wireless localization using RSS measurements," Zenodo, Sep. 12, 2025. [Online]. Available: https://doi.org/10.5281/zenodo.17109218

Ali Mahbas(Member, IEEE) received the B.S. degree in Electronic and Communication Engineering from the University of Technology, Baghdad, Iraq, in 2005, the M.S. degree in Communication Network Planning and Management from the University of Portsmouth, U.K., in 2009, and the Ph.D. degree in Electronic Engineering from the University of Kent, Canterbury, U.K., in 2017. He is currently affiliated with Brunel University London. With over ten years of experience as an engineer and team leader in telecommunications and mobile networks, his research interests span 6G networks, heterogeneous networks (HetNets), the Internet of Things (IoT), mobility management, localization, optical wireless communications (OWC), orthogonal time frequency space (OTFS) modulation, environmental sensing, and device-to-device communications.

John Cosmas(M'1989–SM'2008) received the BEng degree in Electronic Engineering in 1978 from Liverpool University and the Ph.D. degree in 1986 from Imperial College, University of London. He is currently a Professor of Multimedia Systems in the College of Engineering, Design and Physical Sciences at Brunel University London. He is co- Director of the University Research Centre: Intelligent Digital Economy and Society Research Centre (IDEAS) and is an associate editor of IEEE Transactions on Broadcasting. His research interests are concerned with the development of Multimedia Networked Systems applied to Future of Broadcasting, Cellular Communications, 2D/3D digital video/graphics media and the synergies between these technologies towards their application towards the benefit of the smart homes, cities environment, health and societies. He has participated in sixteen EU ICT and two EPSRC funded research projects since 1986 and he has led three of these (CISMUNDUS, PLUTO and 3D MURALE). He has graduated 36 PhD and 4 MPhil students and published over 91 research journal papers and 200 conference papers. His latest research is concerned with management of heterogeneous cellular networks, convergence of cellular and ad-hoc networks, 3D MIMO and efficient Software Defined Networks architectures.

I can bring 35 years of experience teaching at British Universities (Queen

Mary University of London and then Brunel University) Digital Electronics and Communications. I have been an IEEE member since 1989 and a BTS member since 2006 during which I have actively participated as an Associate Editor for the IEEE Transactions in Broadcasting and annually attend the BTS IEEE Broadband Multimedia Systems and Broadcasting conference. Through this conference I have introduced many of my research students and academic colleagues to BTS many of whom have subsequently joined the Society and made strong contributions as associate editors, journal and conference contributors. I have organised an IEEE Broadband Multimedia Systems and Broadcasting conference 2013 in London and a BTS IEEE BTS Young Professionals Conference in 2019. I feel that I repay something back in the form of service to the BTS society that has been such a good influence and generous supporter of in my career and within whom I have made many good international friends.

Nila Nilavalan.(Senior Member, IEEE) Prof R. Nilavalan received the B.Sc. Eng in electrical and electronics engineering from University of Peradeniya, SriLanka in 1995 and PhD in Radio Frequency Systems from University of Bristol, Bristol, UK in 2001. From 1999 to 2005 he was a research associate at the then Centre for Communications Research (CCR) and department of medical physics, University of Bristol, UK. He joined the department of Electronic and Electrical engineering, Brunel University, London as a lecturer in 2005 and currently a professor of Electronics (RF & Wireless Comms.). He leads a research group on RF and microwave systems at Brunel university of London. His research involved wireless communication and radio frequency systems and has worked on the use of post reception synthetic focussing concepts for near-field imaging radar for landmine detection and medical applications.. Prof Nilavalan was a member of the European commission, Network of Excellence on Antennas (2002 - 2005), senior member of the IEEE, fellow of the IET and a fellow of the higher education academy.

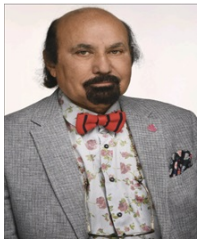

HAMED AL-RAWESHIDY.(Senior Member, IEEE) received the Ph.D. degree from Strathclyde University, Glasgow, U.K., in 1991. He is currently a professor in communications engineering. He was with the Space and Astronomy Research Centre, Iraq, PerkinElmer, USA, Carl Zeiss, Germany, British Telecom, U.K., Oxford University, Manchester Metropolitan University, and Kent University. He is also the Group Leader of the Wireless Networks and Communications Group (WNCG) and the Director of PG studies (EEE) with Brunel University London, U.K. He is the Co-Director of the Intelligent Digital Economy and Society (IDEAS); the new research centre which is a part of the Institute of Digital Futures (IDF). He is a course director for the MSc Wireless Communication and Computer Networks. He is an Editor of the first book in Radio over Fibre Technologies for Mobile Communications Networks. He acts as a consultant and involved in projects with several companies and operators, such as Vodafone, U.K.; Ericsson, Sweden; Andrew, USA; NEC, Japan; Nokia, Finland; Siemens, Germany; Franc Telecom, France; Thales, U.K. and France; and Tekmar, Italy, Three, Samsung and Viavi Solutions—actualizing several projects and publications with them. He is a Principal Investigator for several EPSRC projects and European Project, such as MAGNET EU Project (IP) 2004-2008. He has published more than 500 journals and conference papers and his current research interests include 6G with AI and Quantum and the IoT with AI and Quantum. He is also an External Examiner for the Beijing University for Posts and Telecommunications (BUPT)—Queen Mary University of London. Further, he was an External Examiner for a number of the M.Sc. communications courses with Kings College London, from 2011 to 2016. He has also contributed to several white papers. Specifically, he was an Editor of Communication and Networking (White Paper), which has been utilised by the EU Commission for research. He has been invited to give presentations at the EU workshop and delivered two presentations at Networld2020, and being the Brunel Representative for NetWorld2020 and WWRF (for the last 15 years).